Idealized simulations of wind farm interactions with intermittent turbulence in stable boundary layer conditions

Adam S. Wise[1,2], Robert S. Arthur[2], Jeffrey D. Mirocha[2], Julie K. Lundquist[3,4], and Fotini K. Chow[2]

[1]Department of Civil and Environmental Engineering, University of California, Berkeley, California 94720 USA
[2]Lawrence Livermore National Laboratory, Livermore, California 94550 USA
[3]Johns Hopkins University, Baltimore, Maryland 21218 USA
[4]National Renewable Energy Laboratory, Golden, Colorado 80401 USA

Correspondence: Adam S. Wise (wise14@llnl.gov)

Abstract. Stable atmospheric boundary layer conditions typically correspond to low turbulence levels, but intermittent periods of elevated turbulence can occur during otherwise quiescent conditions. The interaction between intermittent turbulence and wind turbines is not well understood because of sparse observations, as well as the difficulty in realistically resolving small-scale turbulence during strongly stable conditions with numerical simulations. In this study, an explicit filtering and re-

5 construction approach for large-eddy simulation (LES) is used to simulate weakly and strongly stable conditions, with surface cooling rates of -0.2 and -2.0 K h^{-1}, respectively. This approach can sustain resolved background turbulence at relatively coarse grid spacing and stronger stratification compared to conventional closures, resulting in more realistic intermittent stable boundary layer (SBL) turbulence. The idealized LES capability of the Weather Research and Forecasting model is employed with turbine rotors parameterized using generalized actuator disks to 1) determine how the presence of turbine wakes affects

10 SBL evolution, and 2) examine the effect of intermittent turbulence on power production and wake recovery. Wakes increase mixing and therefore increase the height of the SBL, with this effect becoming more prominent as SBL strength increases. Intermittent turbulence does not have a significant impact on mean power generation and wake recovery because the relevant turbulent structures in this study only affect the bottom half of the rotor disk. Power production is, however, more variable during periods of elevated turbulence, demonstrating the impact of SBL intermittency. This study uses an idealized configu-

15 ration, focusing on LES model performance and physical understanding, with the goal of informing future simulations of the conditions observed during the American Wake Experiment.

1 Introduction

Onshore wind turbines experience the stable atmospheric boundary layer nearly every night. Stably stratified flows occur as the earth's surface cools in the absence of radiation from the sun. The associated buoyancy suppression results in small-scale

20 and sometimes intermittent turbulence, which can be difficult to capture in numerical models. This relatively small-scale and low-amplitude ambient turbulence, especially when compared to daytime convective conditions, results in wind turbine and farm wakes sometimes persisting over 30 rotor diameters (D) downwind (Hirth and Schroeder, 2013), which can be over 4 km depending on the turbine type. Additionally, turbine fatigue damage is highly correlated with strong vertical wind shear,

periods of elevated turbulence, and wave-like motions, all of which are common in the stable boundary layer (SBL) (Sisterson
and Frenzen, 1978; Mahrt, 2014). Representation of stably-stratified turbulence is therefore critical when modeling wind farms
to characterize and predict performance.

Wind turbine performance during nocturnal stable conditions is highly dependent on many factors, including the strength of
stability, as well as the presence of waves and intermittency. Low-level jets (LLJs), which are occur frequently during stable
conditions, can increase turbulence intensity and intermittency, as well as mean shear and veer profiles. For weak stability,
shear production overcomes buoyancy and turbulence is continuous in the SBL. However, for strong stability, turbulence can
be suppressed or become intermittent.

The definition of "intermittent turbulence" varies in the published literature owing to its applicability to a range of SBL
phenomena. Perhaps most simply, Mahrt (2014) defines intermittency as "strong variability of the turbulence in space and
time." Many observed SBL phenomena can be described as intermittent. More technically, turbulence intermittency in the at-
mosphere has been broken down into two main categories (Mahrt, 1989, 1999). Mahrt (1989) defines *small-scale intermittency*
as a substructure of the main coherent eddies in a flow and *global intermittency* as the patchiness of turbulence on scales larger
than the main eddies. Global intermittency can be broken down further into two types: external and internal. External intermit-
tency is cause by nonstationary submesoscale motions, whereas internal intermittency is caused by shear instability (Mahrt,
2014). Examples of nonstationary submesoscale motions that trigger external intermittency include breaking gravity waves,
bores, Kelvin-Helmholtz billows, terrain-induced flows, and propagating density currents (Rottman and Simpson, 1989; Sun
et al., 2002; Banta, 2008; Mahrt, 2014). Conversely for internal intermittency, shear increases locally, inducing instability and
mixing (Mahrt, 2014; Sun et al., 2015). Internal intermittency can be a cyclic process as mixing leads to decreased shear and
turbulence decay, but as shear eventually builds back up, instability occurs again. This process tends to occur during strongly
stable conditions due to the high shear requirement. It is sometimes referred to as the upside-down SBL because the most
energetic turbulence is generated by shear aloft rather than by shear in the near-surface region (Mahrt, 1985, 1999; Sun et al.,
2002; Banta, 2008).

Internal intermittency is the main focus of this study, and is quantified following Coulter and Doran (2002), who used
turbulent heat fluxes from sonic anemometer and meteorological tower data during the Cooperative Atmospheric Surface
Exchange Study (CASES-99) to calculate an "intermittency fraction." Note that, here, we extend their quantification method
from turbulent heat flux to turbulence kinetic energy, which is the primary focus of our analysis. The intermittency fraction is
based on the cumulative distribution of the turbulent quantity during an analysis period. A threshold is determined as the value
at which 50% of the cumulative distribution function is reached. Periods with the turbulent quantity greater than the threshold
are considered active 'bursts' or turbulent. On intermittent nights, Coulter and Doran (2002) found intermittency fractions
between 15% and 30%, which for a 12-hour nighttime period means that the majority of the turbulence occurs over a window
of just 1.8 to 3.6 hours.

There are a number of other methods to quantify intermittency available in the literature. For example, Holtslag and Nieuw-
stadt (1986) proposed a scaling condition based on the boundary layer height, the altitude within the boundary layer, and
the Obukhov length. However, this scaling condition is not designed to determine when flow is turbulent or quiescent in a

time-dependent sense. van der Linden et al. (2020) defined time periods as turbulent when the horizontally averaged kinematic temperature flux at the top of the boundary layer in their simulations became greater than the surface temperature flux. In their study, they found an intermittency fraction of roughly 26%, similar to those observed by Coulter and Doran (2002). Ultimately, we follow Coulter and Doran (2002) as their method is observation-based but can be easily applied to simulation datasets. For example, their method could be applied to the observational network at the American Wake Experiment (AWAKEN) in future analyses.

Intermittent turbulence in the SBL can affect turbine power production, wake recovery, and structural loading. Among the goals of the recent AWAKEN field campaign is to investigate the role of intermittent turbulent bursting events on wind farm power production and the structural loading of wind turbines (Moriarty et al., 2020, 2025). The AWAKEN field campaign serves as the inspiration for the present study, which focuses on idealized flow and flat terrain to better understand intermittent turbulence interactions with wind farms. We simulate weak and strong stability conditions to study the interaction between wind turbines and the SBL, to 1) determine how the presence of wind turbine wakes affects stable boundary layer evolution, and 2) examine the effect of intermittent turbulence on power production and wake recovery.

To answer these questions, we use large-eddy simulation (LES); however, there have been a number of LES studies that demonstrate the dependence of simulation results in SBL conditions on the turbulence closure scheme. Beare et al. (2006) found that at a moderate grid spacing (6.25 m), mean profiles were highly dependent on the turbulence closure; however, at fine resolutions of 2 m or less, there were only small changes in mean profiles. Zhou and Chow (2011) modeled a range of SBLs, comparing the common turbulence kinetic energy order-1.5 (TKE-1.5) closure (Deardorff, 1980) and the dynamic reconstruction model (DRM) (Chow et al., 2005) at various grid resolutions in idealized conditions. Unlike the TKE-1.5 closure, the DRM closure accounts for backscatter, or the transfer of energy from the subfilter scale to resolved scales, which Zhou and Chow (2011) found to improve the representation of near-surface profiles under moderate and strong ($\sim$2.0 K h^{-1}) stability conditions. As a result, the DRM closure was able to sustain resolved turbulence and better represent mean shear and potential temperature profiles at coarser resolutions ($\Delta x, \Delta z = 8$ m, 2.5 m and $\Delta x, \Delta z = 16$ m, 5 m) compared to the TKE-1.5 closure, which needed grid spacing as fine as $\Delta x = \Delta z = 3.125$ m. The DRM closure was also used to simulate a real case of intermittent turbulence during the CASES-99 field campaign (Zhou and Chow, 2014). Zhou and Chow (2014) used a multi-scale nested setup with a horizontal grid spacing of 25 m on the finest (LES) domain. They found that intermittent turbulence could be generated through gravity wave breaking over a cold-air pool in a valley upwind of measurements. However, wave breaking only occurred in the simulations when using the DRM closure.

In this study, we use LES and the DRM turbulence closure to simulate weak and strong SBL conditions with a wind turbine parameterization (Sec. 2) to comprehensively explore a range of SBL interactions with a wind farm. This builds on a number of previous studies in the literature, which have used idealized LES to examine certain SBL conditions for modeling wind turbine and wind farm flows (Lu and Porté-Agel, 2011; Marjanovic et al., 2017; Gadde and Stevens, 2021b; Sanchez Gomez et al., 2023), as well as other studies that have proven the efficacy of the DRM closure for capturing intermittent turbulent events (Zhou and Chow, 2011, 2014; Wise et al., 2025). First, we analyze the effect of the turbulence closure on SBL development for both regimes (Sec. 3.1). Then, because the strongly stable regime is intermittently turbulent, we quantify intermittency

(Sec. 3.2). Lastly, we analyze the interaction between the wind farm and different SBL conditions focusing on wind farm power production (Secs. 3.3 and 3.4), followed by conclusions and recommendations for future work (Sec. 4).

2 Methods

2.1 WRF-LES-GAD

To study wind farm performance in a range of SBL conditions, we use the LES capability of the WRF model (Skamarock et al., 2021), version 4.4, with a generalized actuator disk (GAD) (Mirocha et al., 2014b), hereinafter referred to as WRF-LES-GAD. The GAD model implemented in WRF follows blade element momentum theory and requires specifications for the turbine's airfoil lift and drag coefficients. These coefficients come from a 1.6 megawatt (MW) wind turbine parameterization used in Arthur et al. (2020), which has a 80-m hub-height and 80-m rotor diameter (D). This GAD implementation typically requires a grid spacing of at least 10 m to capture the effect of the rotor drag on the resolved flow (Mirocha et al., 2014b, 2015; Arthur et al., 2020; Wise et al., 2022; Sanchez Gomez et al., 2022, 2023).

Our WRF-LES-GAD build also includes a modified surface layer implementation (Mirocha et al., 2015) which iteratively solves for velocities and temperature at the first grid point above the surface using Monin-Obukhov similarity theory (MOST) (Monin and Obukhov, 1954). WRF's native MOST implementation only allows a surface heat flux condition to be specified; the modified surface layer scheme allows a cooling rate to be specified and calculates the surface heat flux and friction velocity based on universal functions for MOST (Businger et al., 1971). It is worth mentioning that MOST is based on the assumption of continuous turbulence. While the validity of MOST for strongly stable regimes is questionable (Optis et al., 2014), the present work aims to extend the capabilities of the model to very stable stratification as there are not any other proven methods for more accurately treating the bottom boundary condition in strongly stable regimes.

LES uses a spatial filter to separate the larger resolved scales from the subfilter-scale (SFS) motions. This filter can be implicit - based on the grid scale, or explicit. The effects of the SFS scales on the resolved scales are then parameterized using a turbulence model. As stability increases, the energetic turbulent motions become smaller and smaller, requiring a finer grid to resolve them. The most common LES schemes use an eddy-viscosity model with no explicit filter to relate SFS and resolved motions. These models are entirely dissipative with energy transfer from larger scales to smaller scales; however, energy transfer from small to large scales can be important, especially in stably stratified environments (Sullivan et al., 2003). More sophisticated turbulence closures are able to account for this backscatter of energy using an explicit filtering approach. Here, we use the dynamic reconstruction model (DRM) of Chow et al. (2005) to extend the working range of LES and to analyze turbine-airflow interactions in more stably stratified flows. Comparisons are also made to the commonly-used turbulent kinetic energy order-1.5 model (TKE-1.5) (Deardorff, 1980), which solves a prognostic TKE equation with a grid-based length scale to define the eddy viscosity.

2.2 Dynamic reconstruction turbulence model

125 The dynamic reconstruction model uses a 3D filter applied to the Navier-Stokes equations to separate large and small scales. This filter is twice the grid cell spacing and is applied explicitly in the model; it is thus distinct from the implicit effects of grid discretization. The effect of the implicit grid filter, as well as numerical truncation errors, is to prohibit motions smaller than the grid scale. There is thus a range of scales between the grid scale and the filter scale that can be partially reconstructed in the model.

130 The governing equations of LES on a discrete grid are:

$$\frac{\partial \overline{\tilde{u}}_i}{\partial t} + \frac{\partial \widetilde{\overline{\tilde{u}}_j \overline{\tilde{u}}_i}}{\partial x_j} = -\frac{1}{\rho}\frac{\partial \overline{\tilde{p}}}{\partial x_i} + \nu \frac{\partial^2 \overline{\tilde{u}}_i}{\partial x_i \partial x_j} - \frac{\partial \tilde{\tau}_{ij}}{\partial x_j} + \tilde{F}_i \tag{1}$$

where x_i represents the x, y, and z spatial dimensions, u_i are velocities, p is pressure, ρ is density, τ is the turbulent stress, and $\tilde{F}_i$ represents a body force (such as drag from a wind turbine rotor). The overbar operator represents a filtered field via a smooth spatial filter and the tilde operator represents a resolved and unfiltered field. The operators combined represent a resolved and

135 filtered field, thus $\overline{\tilde{u}}_i$ is the resolved, filtered velocity. See Chow et al. (2005) for more details on the notation.

The full turbulent stress term is referred to as the subfilter-scale stress (τ^{SFS}) which is made up of two components, a resolvable subfilter-stress (RSFS), τ^{RSFS}, and a subgrid-scale (SGS) stress, τ^{SGS}:

$$\tau^{SFS} = \tau_{ij} = \tau^{SGS} + \tau^{RSFS} = \left(\overline{u_i u_j} - \overline{\tilde{u}_i \tilde{u}_j}\right) + \left(\overline{\tilde{u}_i \tilde{u}_j} - \overline{\tilde{u}}_i \overline{\tilde{u}}_j\right) \tag{2}$$

The RSFS term represents the range of eddy motions between the implicitly defined grid filter (i.e., the Nyquist limit) and the
140 explicit LES filter. When an explicit filter is defined, τ^{RSFS} is resolvable on the grid, but this term is generally ignored in conventional turbulence closures which only parameterize SGS stresses.

For the DRM closure, the subgrid scale stress, τ^{SGS} is parameterized using the Dynamic Wong-Lilly (DWL) (Wong and Lilly, 1994) eddy-viscosity model:

$$\tau^{SGS} = -2\nu_t \overline{\tilde{S}}_{ij} \tag{3}$$

145 where $\overline{\tilde{S}}_{ij}$ is the filtered and resolved strain rate tensor and $\nu_t = C_\epsilon \Delta^{4/3}$ is the dynamic eddy viscosity. Here, Δ is the filter width, and $C_\epsilon \Delta^{4/3}$ is determined dynamically using the least-squares method of Lilly (1992).

The RSFS stress is determined by reconstructing the velocity field using the approximate deconvolution method (Stolz et al., 2001):

$$\tilde{u}_i \approx \overline{\tilde{u}}_i + (I - G) * \overline{\tilde{u}}_i + (I - G) * \left[(I - G) * \overline{\tilde{u}}_i\right] + \dots \tag{4}$$

150 where I is the identity matrix, G is the explicit filter and $*$ represents the convolution operator. Each additional term in the series adds a level of reconstruction that more accurately represents the RSFS velocities. In this study, level-0 reconstruction is used which includes the first term in the series, and the velocity is approximated as the filtered velocity. This level-0 reconstruction is the same as the scale-similarity model of Bardina (Bardina et al., 1983). Combined with the eddy viscosity SGS term, this

level-0 reconstruction becomes a dynamic mixed model (Zang et al., 1993). Higher levels of reconstruction have been the
155 focus of other studies (Zhou and Chow, 2011; Simon et al., 2019), with increasing levels restoring turbulent scales near the
filter cutoff (Zhou and Chow, 2011); however, we focus on level-0 reconstruction as it results in the biggest benefit with the
least added computational cost. We refer to the closure as DRM for simplicity and to indicate the more general implementation
in WRF.

Lastly, near-wall stresses are usually under-predicted with dynamic SGS models applied in ABL flows (Chow et al., 2005).
160 A near-wall stress model (Brown et al., 2001) is used to account for this, which has improved agreement with similarity theory
in previous studies (Chow et al., 2005; Zhou and Chow, 2011, 2012; Kirkil et al., 2012). The near-wall stress is defined for
$i = 1, 2$ and is added only to the τ_{i3} terms, as follows:

$$\tau_{i3}^{\text{near-wall}}(z) = - \int C_c a(z) |\overline{\tilde{u}}| \overline{\tilde{u}}_i dz \tag{5}$$

where C_c is a strength factor, set to 0.5 due to the grid-aspect ratio in this study, and $a(z)$ is a shape function set to smoothly
165 decay the effect of the canopy stress at a specific cutoff height H_c (Chow et al., 2005; Kirkil et al., 2012). H_c is chosen as $2\Delta x$
following Zhou and Chow (2011). The shape function is defined as:

$$a(z) = \cos \left(\frac{\pi z}{2H_c} \right)^2 \tag{6}$$

The DWL eddy-viscosity model and the scale-similar RSFS term are combined to create a mixed-model for turbulence. This
mixed model along with the added canopy stress result in:

$$170 \quad \tau_{ij} = \tau^{RSFS} + \tau^{SGS} = \overline{\overline{\tilde{u}_i \tilde{u}_j}} - \overline{\tilde{u}}_i \overline{\tilde{u}}_j - 2C_\epsilon \Delta^{4/3} \overline{\tilde{S}}_{ij} + \tau_{i,\text{near-wall}} \tag{7}$$

With the DRM's formulation for RSFS motions, subfilter-scale turbulent dissipation $\epsilon = -\tau_{ij} \overline{\tilde{S}}_{ij}$ can vary both positively
and negatively representing dissipation and backscatter. It is worth noting that in conventional closures, such as TKE-1.5, the
eddy-viscosity form is purely dissipative. This is because the SFS stress does not represent RSFS motions and only encom-
passes SGS motions, resulting in ϵ being strictly positive.

175 The SFS scalar fluxes in the DRM follow a similar procedure to momentum. The SFS fluxes are comprised of two terms,
the SGS, eddy-diffusivity contribution from the DWL model and the RSFS contribution from the approximate deconvolution
method. The SFS potential temperature, θ, flux in the DRM model is:

$$\tau_{\theta j} = \underbrace{\overline{\overline{\tilde{\theta} \tilde{u}_j}} - \overline{\tilde{\theta}} \overline{\tilde{u}}_j}_{\tau_{\theta j}^{RSFS}} \underbrace{- 2\nu_{t,h} \frac{\partial \overline{\tilde{\theta}}}{\partial x_j}}_{\tau_{\theta j}^{SGS}} \tag{8}$$

where $\nu_{t,h}$ is the dynamic, scalar eddy diffusivity defined as $\nu_{t,h} = \nu_t / Pr$ with $Pr = 1/3$ as defined in WRF (Skamarock
180 et al., 2021).

2.3 Turbulent kinetic energy 1.5-order model

The TKE-1.5 model is an eddy-viscosity turbulence closure which solves a prognostic turbulent kinetic energy (TKE) equation to obtain a characteristic turbulent velocity scale and uses the grid spacing as the length scale to parameterize the SGS stresses (the RSFS term is not included). The TKE equation describes the evolution of TKE and parameterizes sources and sinks from shear production, buoyancy production or suppression, turbulent mixing, and dissipation (Skamarock et al., 2021). The eddy-viscosity is defined as:

$$\nu_t = C_k l_{h,v} e^{1/2} \tag{9}$$

where e is the TKE and C_k is a constant (set to 0.15). The length scales are defined anisotropically with the horizontal length scale defined as $l_h = (\Delta x \Delta y)^{1/2}$ with $\Delta x, \Delta y$ representing the grid spacing in the corresponding direction. The vertical length scale depends on the Brunt-Väisälä frequency, N, and is given by:

$$l_v = \begin{cases} \min\left[\Delta z, 0.76\frac{e^{1/2}}{N}\right] & : N^2 > 0 \\ \Delta z & : N^2 \leq 0 \end{cases} \tag{10}$$

The scalar eddy diffusivity is defined for TKE-1.5 in the same way as the SGS component of the DRM model above:

$$\tau_{\theta j} = -2\nu_{t,h}\frac{\partial\bar{\bar{\theta}}}{\partial x_j} \tag{11}$$

2.4 Simulation setup

WRF-LES-GAD is used in a one-way nested and flat terrain setup to study how a range of SBL conditions interact with a wind farm. The wind farm's inflow conditions are based on the outer domain, which is periodic and unaffected by the turbine wakes (due to one way nesting, wakes are confined to the inner domain). The outer domain size is $(Nx, Ny, Nz) = (750, 500, 120)$, which at a horizontal grid spacing of 8 m results in a physical domain size 6.0 km $\times$ 4.0 km $\times$ 1.0 km ($x \times y \times z$). The inner domain has the same resolution as the outer domain, but has two fewer grid points in x and y to ensure that the inner domain fits within the outer domain. The outer domain with periodic boundary conditions is spun up for 12 hours, then the inner domain with a 3 $\times$ 3 array of wind turbines (see Fig. 1) is nested within the outer domain. The combined nested domains are then run for 2 hrs. The total simulation time is 14 hours for the outer domain and 2 hours for the inner domain, with all analysis completed from hour 13 to 14. This is a computationally efficient approach which allows for turbulence to develop and for the surface fluxes to become pseudo-steady on the periodic outer domain while also accounting for a 1 hr spin-up period of the turbine wakes on the inner domain. This minimal nesting setup has been previously used by Sanchez Gomez et al. (2023) to allow for the study of blockage in front of a wind farm in the inner domain using turbulence developed from an outer domain with periodic boundary conditions.

Distinct wind farm configurations are used for each cooling rate to account for changes in wind direction at hub height. As discussed below, the wind direction varies significantly with height (wind veer) in the stable boundary layer and therefore
210   produces very different wind directions at hub height for different stability conditions, even with the same geostrophic forcing. The 3×3 wind farm is therefore aligned with the hub-height wind direction (known a priori from the outer grid spinup) for each test case as shown in Fig. 1, to maximize efficiency in the computational domain. The turbines are spaced 320 m or $4D$ in the spanwise direction and $8D$ in the streamwise direction. For the weakly stable configuration, the edge of each wind farm is located 800 m from the western and southern boundaries, i.e., the closest any turbine gets to a boundary is 800 m. For the
215   strongly stable configuration, the closest turbine to the western boundary is also 800 m, however, the distance between the closest turbine and the southern boundary is increased from 800 m to 1200 m to account for the extreme wind veer. Figure 1 also shows points $5D$ upwind of the first row of turbines, as well as $5D$ and $10D$ downwind of the third row of turbines where u, v, w, and T are output at all vertical levels at the model time-step meant to represent a virtual meteorological tower or vertical profiling lidar. Spanwise transects $10D$ or 800 m wide are also shown in Fig. 1 at various locations, which are used for
220   analysis later in this work.

The simulations are forced with a geostrophic wind speed of $U = 10$ m s^{-1}, $V = 0$ m s^{-1}, which is typical in idealized studies (Kirkil et al., 2012; Zhou and Chow, 2011; Jiménez and Cuxart, 2005; Mirocha et al., 2014a). The two surface cooling rates used are -0.2 and -2.0 K h^{-1} to represent weakly and strongly stable conditions. These cooling rates fall within the range used by Zhou and Chow (2011) who modeled weakly to strongly stable conditions. The grid has 8 m horizontal spacing and a
225   vertical spacing of 2.5 m near the surface, with a gradual increase in spacing with height. These spacings are chosen because previous research has shown that the DRM is able to sustain resolved turbulence on this grid (Zhou and Chow, 2011). The 8 m grid spacing is also close to the moderate, 6.25 m spacing used in the SBL LES studies by Beare et al. (2006), which was shown to provide reasonable accuracy but with high dependence on the turbulence closure.

At the bottom boundary, surface cooling is prescribed using Monin-Obukhov similarity theory. The surface fluxes are de-
230   termined using the constants and relationships from Businger et al. (1971) and the surface roughness, z_0, is set to 0.1 m. This surface roughness is appropriate for low crops with occasional large obstacles, which is characteristic of the AWAKEN site, especially during the summer season (Krishnamurthy et al., 2021). This configuration of the bottom boundary directly follows the methods of Zhou and Chow (2012). The potential temperature profile used for initialization is neutral at 300 K for the first 100 m with stable stratification of 4 K km^{-1} prescribed above. The initial profile is not meant to represent observed meteo-
235   rological conditions but follows common approaches for simulating idealized SBLs with LES (Zhou and Chow, 2011; Peña et al., 2021).

When examining the effect of the turbulence closure model, only the outer domain is analyzed (i.e., wind turbine effects are not included). Additional runs at a horizontal grid spacing of 4 m are performed for both the DRM and TKE-1.5 closures as a reference (See Appendix A). Since turbulence in LES is strongly tied to the grid spacing, this sensitivity study allows us to
240   assess model quality for both grid spacings and turbulence schemes.
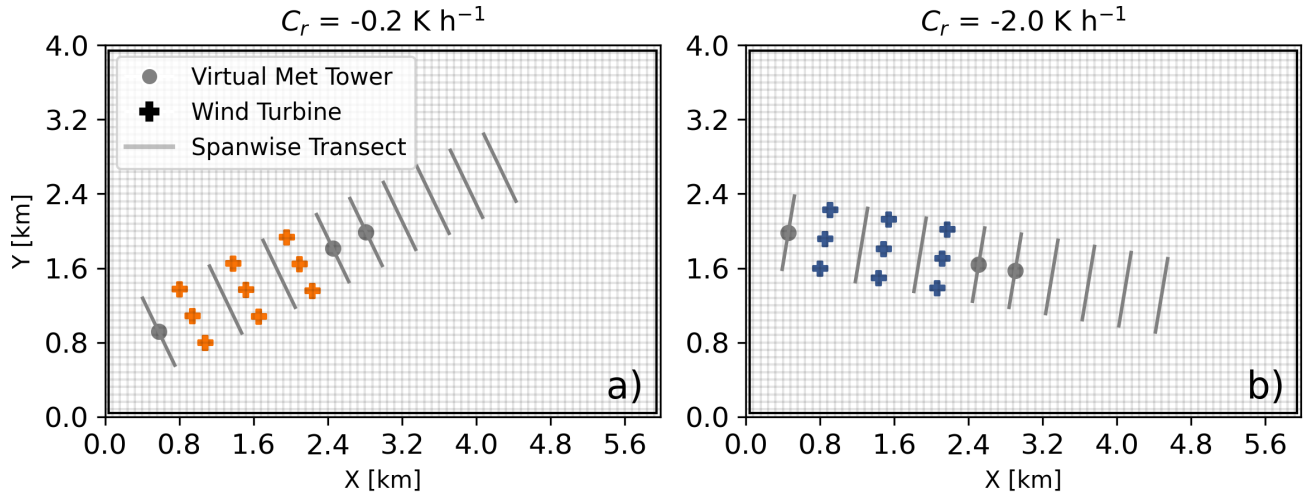
Figure 1. Simulation setup for the (a) weakly and (b) strongly stable regimes denoted by the surface cooling rate C_r. The virtual meteorological tower is located $5D$ upwind of the wind farm and the lines represent $10D$-wide transects at various locations upwind, within, and downwind of the wind farm.

3 Results and discussion

3.1 Effect of turbulence closure

For both regimes, as expected, a low-level jet develops at the top of the SBL. Planar and time-averaged vertical profiles of wind speed, wind direction, and potential temperature are shown in Fig. 2 for the 8 m grid spacing setup. All simulations are run for

245 fourteen hours, and outputs are set to every 30 s during the analysis period from hour 13 to 14 resulting in 120 time-instances in the time average. The simulations using 4 m resolution are very similar but with minor differences in the height of the LLJ (not shown). While 13 hours of surface cooling is not necessarily realistic, selecting an analysis window after this many hours is commonly done in idealized SBL studies (Beare et al., 2006; Gadde and Stevens, 2021a, b; Peña et al., 2021). When the surface is cooled, in LES, it takes many hours until the Coriolis forcing and surface friction balance with super-geostrophic

250 flow at the top of the stable layer. This super-geostrophic flow represents a LLJ (see Fig. 2) and is a phenomenom commonly observed onshore at night (Vanderwende et al., 2015).

The effect of the different cooling rates is clearly observed in the differing LLJ heights. The wind speed profiles are very strongly sheared and become super-geostrophic at the top of the SBL. The maximum wind speed within the low-level jet is close to 12 m s^{-1} for both cases with this maximum occurring at 290 m for the weakly stable regime and 70 m for the strongly
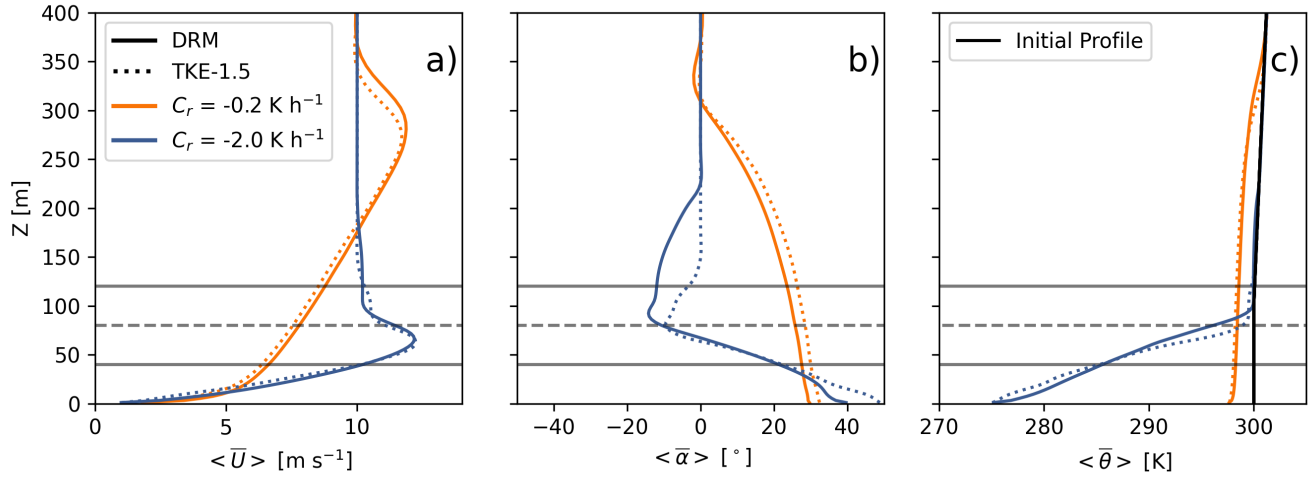
Figure 2. Planar- and time-averaged vertical profiles of (a) wind speed U, (b) wind direction α, and (c) potential temperature θ for the DRM and TKE-1.5 closures at 8 m resolution. Note that results shown are for the outer domain without wind turbines. The solid horizontal lines represent the bottom and top of the rotor layer while the dashed line represents hub-height.

stable regime. While the wind speed at the nose of the LLJ is similar in both cases, the 80-m hub-height wind speed varies greatly due to the shear. The hub-height wind speed is 7.5 m s^{-1} for the weakly stable regime and 12.0 m s^{-1} for the strongly stable regime. The wide range of wind speeds across the rotor swept area leads to differing wake effects (see Sec. 3.4). Another contributing factor to wake behavior is the wind veer, which is nearly 40 degrees across the rotor swept area for the strongly stable regime, but only 5 degrees for the weakly stable regime. This difference has a strong effect on the lateral spreading of turbine wakes as discussed later, when the GAD is added on the inner nest to represent the turbines.

The thermally stable boundary layer develops as a strong potential temperature gradient forms from the ground up to the free atmosphere. In the free atmosphere, the 4 K km^{-1} gradient initially imposed above 100 m persists due a lack of turbulent mixing in the upper atmosphere. The temperature profiles with the different cooling rates are shown in Fig. 3(b), with the surface cooling over 26 K for the strongly stable regime but less than 5 K for the weakly stable case. The height of the stable layer depends on the cooling rate and the choice of the turbulence model, with the stable layer being deeper for the DRM closure compared to the TKE-1.5 closure. This difference is consistent with previous comparisons of the TKE-1.5 and DRM closures in the SBL (Zhou and Chow, 2012). Additionally, the dependence of SBL height on turbulence closure is documented in the GABLS study (Beare et al., 2006).

Figure 3 shows the planar and time-averaged profiles of heat flux normalized by the heat flux value at the surface. (For the DRM closure, the surface heat flux values are -0.017 and -0.040 K m s^{-1} for the weakly and strongly stable regimes, respectively and for TKE-1.5, the values are -0.012 and -0.041 K m s^{-1}.) The resolved fluxes are small near the surface and the turbulent fluxes are modeled by the turbulence closure. Above this region and within the SBL, the resolved fluxes reach a
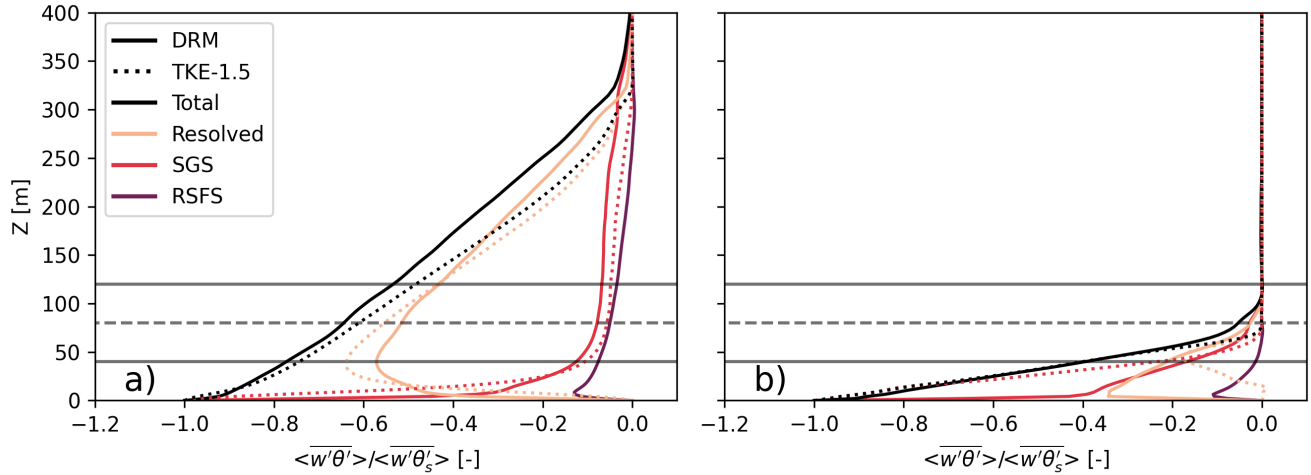
Figure 3. Planar- and time-averaged vertical profiles of normalized heat flux for the (a) weakly stable and (b) strongly stable regime for the DRM and TKE-1.5 closures at 8 m resolution. Note that results shown are for the outer domain without wind turbines. The solid horizontal lines represent the bottom and top of the rotor layer while the dashed line represents hub-height.

maximum and then decrease as buoyancy suppresses turbulence scales. For the weakly stable regime, the differences between two closures is relatively small with both the DRM and TKE-1.5 closures resolving similar amounts of heat flux within the
275   SBL. For the strongly stable regime, a much larger percentage (nearly three times) of the heat flux is resolved in the boundary layer for the DRM closure compared to results with the TKE-1.5 closure. For further analysis on the resolved and model heat fluxes between the two closures and at additional grid resolutions, see Appendix A.

One of the benefits of the DRM is that it allows backscatter of energy from subfilter scales to resolved scales. This effect can be quantified by calculating the SFS dissipation rate $\epsilon = -\tau_{ij}\tilde{\bar{S}}_{ij}$. Figure 4 shows a histogram of the SFS dissipation rates for
280   the TKE-1.5 and DRM closures at heights of 50 m and 80 m above the ground for the 8 m resolution strongly stable regime. As expected, the histograms of dissipation rate are entirely positive for the TKE-1.5 closure because it is an eddy-viscosity model. For the DRM closure, approximately 20% at z = 50 m and 40% at z = 80 m of the SFS dissipation rate values are negative, indicating backscatter. Traditional eddy-viscosity closures are known to be overly dissipative (Carper and Porté-Agel, 2004; Sullivan et al., 2003) and backscatter has been shown to be important, especially in stably stratified flows (Mason and
285   Thomson, 1992; Kosović, 1997). Backscatter was also seen in Zhou and Chow (2011) and matches turbulence measurements in the atmospheric surface layer (Carper and Porté-Agel, 2004).

The ability of the DRM closure to physically represent backscatter leads to an improved representation of turbulence under strong stability compared to the TKE-1.5 closure, especially at the relatively coarse 8 m grid spacing. Figure 5 shows the planar- and time-averaged vertical profiles of the normalized total momentum flux as well as the percentage of backscatter
290   in the SFS dissipation rate as a function of height for the DRM closure for both stability regimes and at 8 m horizontal grid
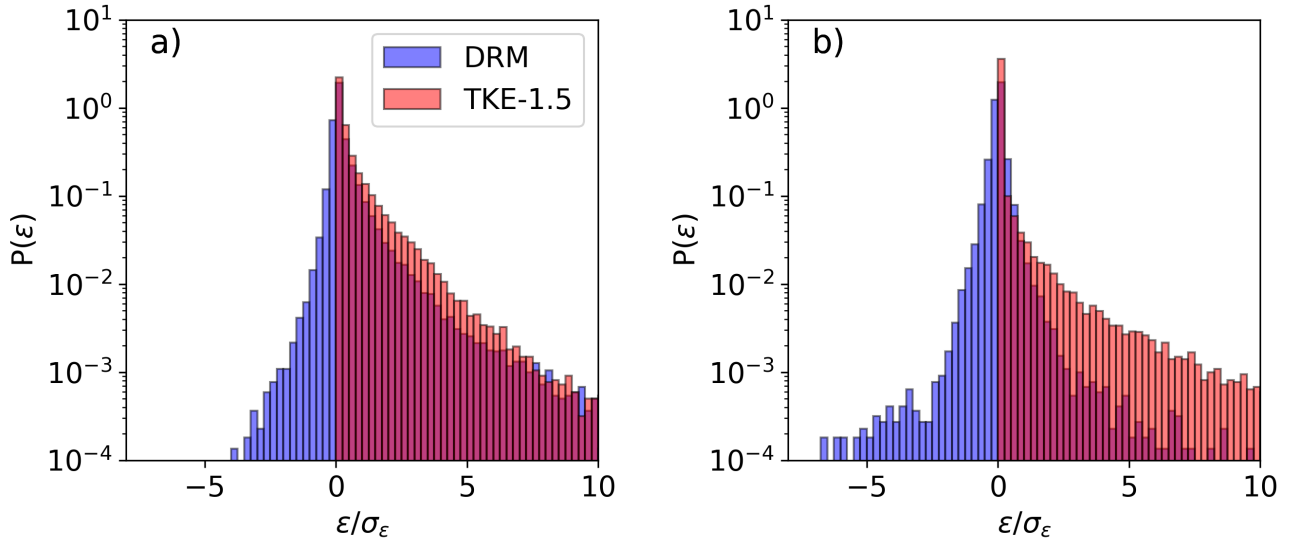
Figure 4. Distribution of subfilter scale turbulent dissipation rates for the TKE-1.5 and DRM closures at (a) z = 50 m and (b) hub-height (z = 80 m) on the outer domain for the strongly stable regimes. The turbulence dissipation rate ϵ is normalized by its standard deviation σ_ϵ at the given height. Negative values represent the backscatter of turbulent energy from the subfilter scales to the resolved scales.

spacing. (The magnitude of the surface momentum flux values are 0.30 and 0.14 $\mathrm{m^2\ s^{-2}}$ for the weakly and strongly stable regimes, respectively.) The momentum flux profiles in Fig. 5 are also shown with conditionally averaging based on the sign of the SFS dissipation. In the strong stability case, local backscatter events (where $\epsilon < 0$) result in larger magnitude momentum fluxes compared to the fluxes in areas of positive SFS dissipation ($\epsilon > 0$). For the weak stability case, the magnitude of the

295 momentum fluxes is more similar for backscatter and dissipation events. Lastly, for both stability regimes, the momentum fluxes at the top of the boundary layer and within the LLJ are of similar magnitude but with opposite signs during backscatter and dissipation events. The fluxes when $\epsilon > 0$ are balanced by the fluxes when $\epsilon < 0$ as the contributions from backscatter and positive SFS dissipation are roughly equal at the top of the boundary layer.

Using the DRM closure at 8 m grid spacing provides a computationally efficient framework for simulating a domain large

300 enough to analyze wind turbine and farm wake effects under strongly stable conditions (see Appendix A for analysis regarding computational cost between the two closures). Hereinafter, all results presented use the DRM closure.

3.2 Quantifying intermittency

There are multiple definition of turbulence intermittency in the atmosphere with this study focusing on global intermittency. Holtslag and Nieuwstadt (1986) remark that for global intermittency, turbulence is weak and sporadic and not continuous in

305 time and space, with turbulence confined to isolated patches that develop and disappear. We use scaling to initially characterize the behavior (continuous vs intermittent) of the simulated stable boundary layers. Holtslag and Nieuwstadt (1986) identified

WIND
ENERGY
SCIENCE
DISCUSSIONS
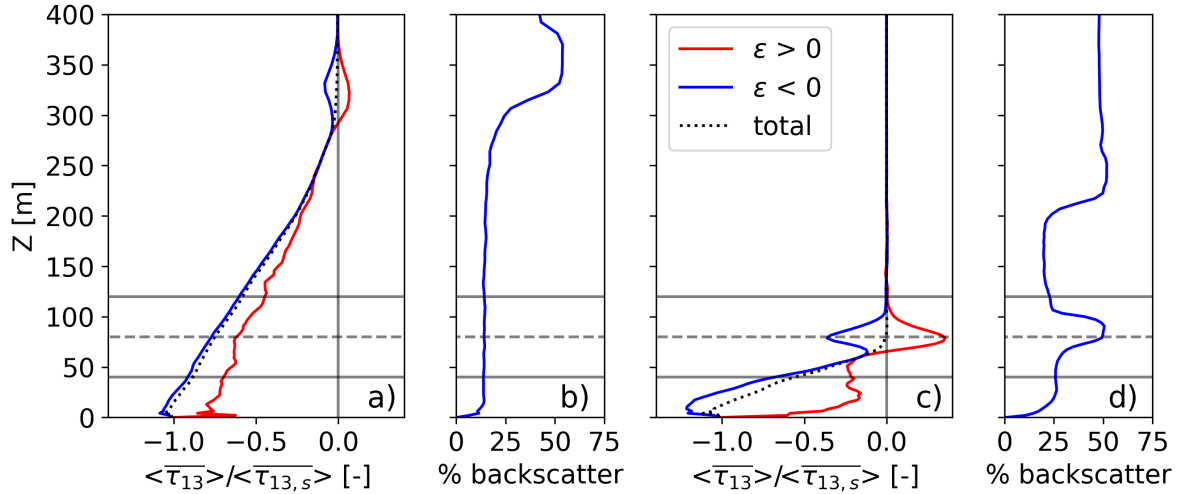
Figure 5. Planar- and time-averaged vertical profiles of normalized total momentum flux (resolved + modeled) for the (a) weakly stable and (c) strongly stable regime for the DRM closure at 8 m resolution conditionally averaged based on the sign of the SFS dissipation rate (negative indicating backscatter). Percentage of backscatter in the SFS dissipation rate for a given height for the (b) weakly and (d) strongly stable regimes. Note that results shown are for the outer domain without wind turbines. The solid horizontal lines represent the bottom and top of the rotor layer while the dashed line represents hub-height.

scaling parameters to define a criteria in which the SBL displays intermittent behavior at a given height. Their criteria depends on the boundary layer height h and the Obukhov length L. The boundary layer height can be determined following their definition, which is the height to which turbulence extends or the height at which the fluxes go to 0. The boundary layer

310 height for the strongly stable regime is determined to be 105 m. The average Obukhov length over the analysis period can be calculated as: $L = -\overline{u_*}^3 \theta / \kappa g \overline{w'\theta'}$, where $\overline{u_*}$ is the time-averaged surface friction velocity, $\overline{w'\theta'}$ is the time-averaged surface heat flux, κ is the von Kármán constant (taken as 0.4), g is the gravitational constant, and θ is the potential temperature at the surface. For the strongly stable regime, the average surface heat flux is -0.040 K m s^{-1} and the average surface friction velocity is 0.14 m^2 s^{-2}. The Obukhov length is calculated as 5.4 m for the strongly stable regime resulting in $h/L = 19$, thus

315 confirming that the strongly stable regime is intermittent as defined by Holtslag and Nieuwstadt (1986). For the weakly stable regime, $h/L = 3$ and is in the region of continuous turbulence. See Holtslag and Nieuwstadt (1986) for additional details on scaling in the SBL.

To quantitatively describe the intermittent turbulence visible in the strongly stable case at a given height, we follow a similar approach to that used by Coulter and Doran (Coulter and Doran, 2002) who used heat flux measurements from sonic

320 anemometer data during the CASES-99 field campaign. We apply their methodology but use TKE as the metric of interest as our goal is to identify turbulent periods. At the virtual tower, the TKE is calculated at each height using 30 s bins, as we are focused on small-scale turbulence, and then averaged again over a 1-min interval to further smooth the data (shown in

Figure 6(a) at various heights). Then the values in the TKE time-series are sorted from largest to smallest to obtain a cumulative probability distribution.

325   The cumulative probability distribution of the sorted TKE at various heights within the rotor plane for the strongly stable regime is shown in Fig. 6(b). The black diagonal line represents the distribution if the TKE were distributed uniformly during the analysis period, i.e., 50% of the TKE would occur in 50% of the analysis period. We extend Coulter and Doran's (Coulter and Doran, 2002) definition of "intermittency fraction" to TKE (from heat flux) such that it represents the first 50% of the sorted TKE signal. It should be noted that TKE cannot be uniformly distributed since it is defined itself by fluctuations, so
330   there will always be some level of skewness and the intermittency fraction must be less than 50%. For the strongly stable regime, the intermittency fraction is 30% at hub-height and 29% at $z = 50$ m, meaning that 50% of the total TKE during the analysis period happens in just 30% of the analysis time. In the upper portion of the rotor plane, the intermittency fraction is closer to 40%. An intermittency fraction of 29% is consistent with the <30% intermittency fractions observed during many of the strongly stable nights analyzed by Coulter and Doran (Coulter and Doran, 2002) during CASES99 (although they also
335   saw nights with smaller intermittency fractions) and simulation results during strongly stable conditions from Zhou and Chow (2012). Similarly, in simulations by van der Linden et al. (2020), they found their SBL regime to be in a turbulent or bursting state 26% of the time although they used a different metric to quantify intermittency. However, note that the results in this study do not provide a direct comparison since TKE is the metric used whereas the others used heat flux.

The analysis period is further subdivided into quiescent and turbulent periods. Figures 6(a) and 6(c) show time-series of the
340   wind speed and TKE at $z = 50$ m, 80 m, and 110 m where periods with intermittency are highlighted in gray and denoted as "turbulent" periods while other periods are referred to as "quiescent" periods. We can qualitatively see large fluctuations in both the wind speed and TKE during the turbulent periods at 50 m. At 80 m (hub-height) and 110 m, the fluctuations are not as qualitatively evident. We use turbulence intensity (TI), calculated as TI = σ_U/U_{mean}, to quantify the differences in turbulence during the quiescent and turbulent periods. At 50 m, the TI is 3.5% during the turbulent periods and only 2.2%
345   during quiescent periods. Considering the relatively small TIs typical during SBL conditions, these differences in TI during quiescent and turbulent periods are significant, as discussed later. Note that at both 80 and 110 m, the wind speed slowly decreases in time due to multi-hour ($\sim$18.7 hours at a latitude of 40 degrees) inertial oscillations at the Coriolis frequency.

Increased levels of turbulence during turbulent periods, as compared to quiescent periods, are also clear when plotting the power spectral density (PSD) of the wind speeds at the three heights as shown in Fig. 6(d). The wind speed signals have been
350   separated by turbulent and quiescent periods as indicated by the gray shaded regions in Fig. 6(c). The PSDs are calculated for each distinct turbulent or quiescent period and then averaged. At 50 m, the energy content is increased across all frequencies during the turbulent periods compared with the quiescent periods. There is a much smaller difference in the energy content at the higher frequencies for heights of 80 m and 110 m. The additional energy content for only the lower-half of the rotor disk along with the intense vertical wind shear could lead to increased blade fatigue (Kelley et al., 2006).

355   The shape of the distribution of turbulence can be used as an additional metric to confirm intermittency in the strongly stable regime. While we expect the distribution for continuous turbulence to be roughly Gaussian (i.e., with one peak), for intermittent turbulence we expect the distribution to be bimodal. Figure 7 shows the time-series of TKE for both the weakly
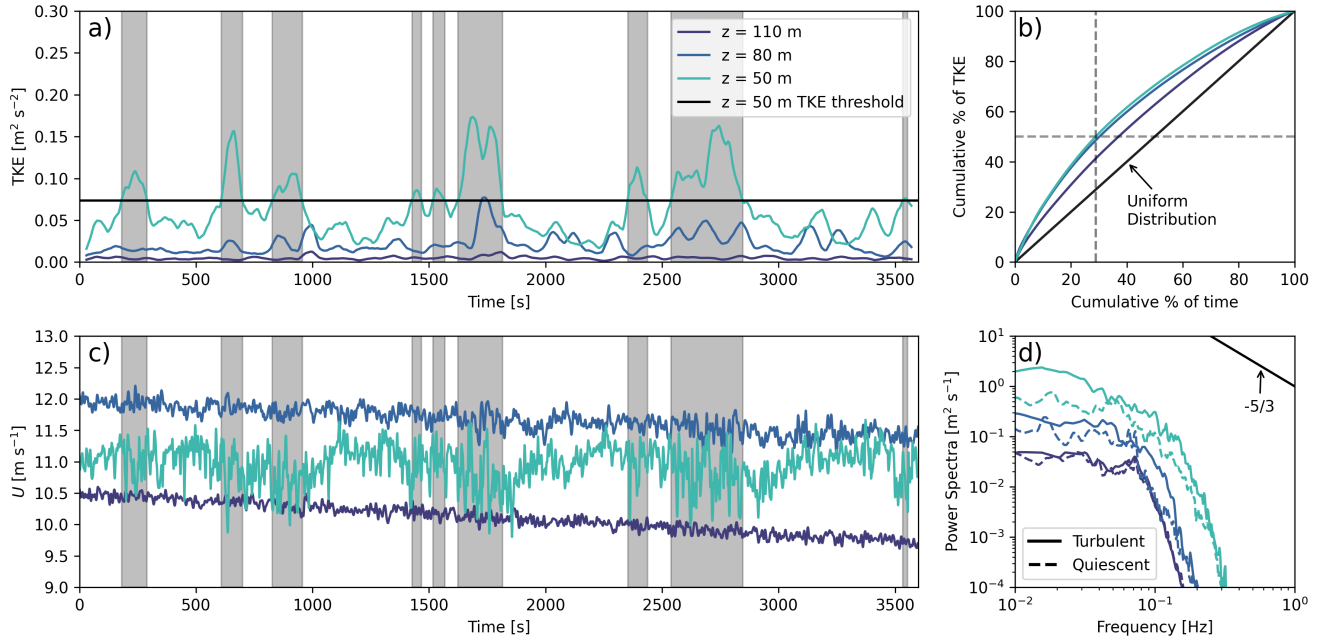
Figure 6. (a) Time-series and (b) CDF of TKE at various heights within the rotor disk for the strongly stable regime $5D$ upwind of the wind farm on the inner domain. (c) Time-series and (d) power spectra of wind speed at the same heights as in (a) and (b). The dashed lines in (b) pinpoint the the cumulative percentage of time it takes until 50% of the TKE occurs at a height of 50 m. The periods highlighted in gray are "turbulent" while other periods are "quiescent".

and strongly stable regimes at 70% of the boundary layer height (50 m above ground level for the strongly stable regime) with the distributions of the TKE signal also provided. As expected for the strongly stable regime, the distribution of turbulence is more bimodal than in the weakly stable regime. The majority of the turbulence occurs around a value of 0.05 m² s⁻¹, with a second, smaller peak around 0.15 m² s⁻¹, which is roughly 3 times as large. To quantify bimodality, we use Sarle's bimodaility coefficient with coefficients larger than 5/9 (0.555) considered to be bimodal (Ellison, 1987). The bimodality coefficient for the distribution of turbulence for the strongly stable regime is 0.63, while it is 0.45 for the weakly stable regime. This result further confirms the intermittent nature of the turbulence in the strongly stable case.

Lastly, plan views of TKE qualitatively demonstrate the spatial organization of intermittent turbulence. Figure 8 shows time instances of TKE at 70% of the boundary layer height at the beginning of the analysis period for the weakly and strongly stable regimes. The TKE is computed as $\text{TKE} = \frac{1}{2}\left(u'^2 + v'^2 + w'^2\right)$, where u', v', and w' are the fluctuating components of the velocities obtained by removing the planar average, e.g., $u' = u - <u>$ where $<u>$ is the planar average for the specific time instance. For the weakly stable regime (Fig 8(a)), the TKE signal exhibits small-scale turbulent structures distributed evenly throughout the domain. When using the DRM closure at a horizontal grid spacing of 8 m, the strongly stable regimes shows patches of increased TKE and more quiescent regions with very little TKE. These patches continuously develop in different
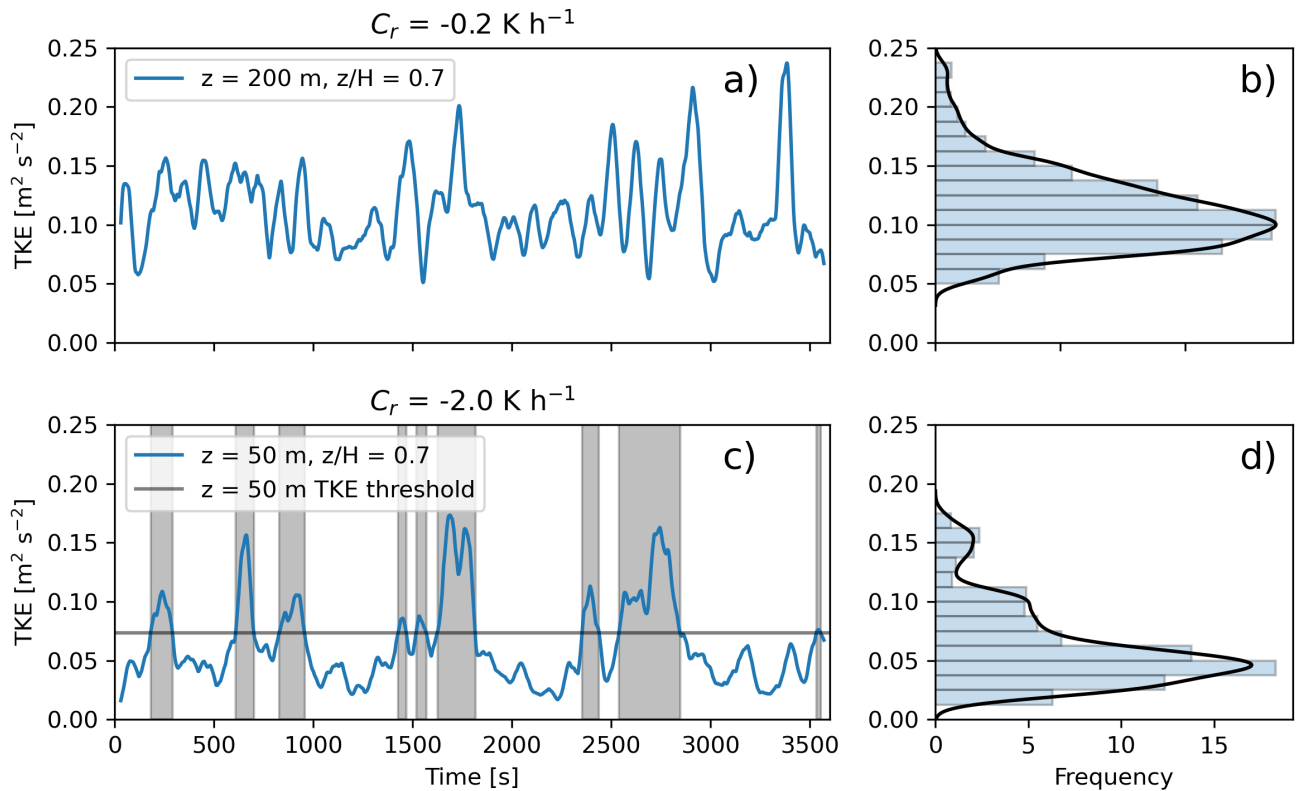
Figure 7. Time-series of TKE at 70% of the boundary layer height for the (a) weakly and (c) strongly stable regimes. Histogram of the TKE distribution for the (b) weakly and (d) strongly stable regimes. The black lines in (b) and (d) represent kernel density estimates of the probability distribution functions. In (c), the periods highlighted in gray are "turbulent" while other periods are "quiescent".

locations throughout the analysis period as result of shear cyclically increasing and decreasing. The patchiness in Fig 8(b) shows qualitative similarities to observations (Mayor et al., 2012) and direct numerical simulations (Ansorge and Mellado, 2014, 2016) of intermittent turbulence.

3.3 Effect of wind farms on the stable boundary layer

The presence of a wind farm has different effects on the atmospheric boundary layer for each stability regime. Figure 9 shows plan views of hub-height instantaneous and time-averaged velocity deficits. The velocity deficit is calculated as the difference in the wind field from the velocity $5D$ upwind of the first row of turbines, with the reference or freestream value being averaged in the spanwise direction (from -$5D$ to $5D$) to account for the width of the farm. In the instantaneous slice in Fig. 9(a), turbulent structures are generally evenly distributed in the weakly stable regimes. For the strongly stable regime in Fig. 9(c), the hub-
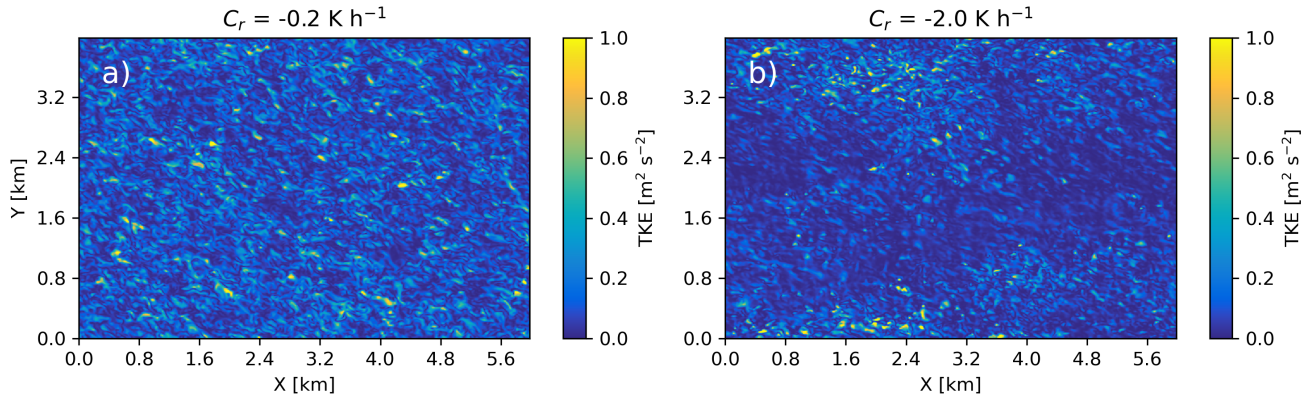
Figure 8. Instantaneous plan view of TKE at the beginning of the analysis period for the (a) weakly stable regime at 200 m above ground level and (b) strongly stable regime at 50 m above ground level. Note that both heights correspond to 70% of the boundary layer height for each regime.

height is just above the nose of the LLJ and thus, much less turbulence is expected. For the instance shown in Fig. 9(c), there are no turbulent structures in the inflow other than some very faint wave-like structures.

For both regimes, the wind turbine wakes propagate over $30D$ downwind as seen in the time-averages in Figs. 9(b) and 9(d). The considerable wind veer also results in the lateral spreading of the wakes, which depends on wind directions at heights where

385 momentum is entrained from as discussed by van der Laan and Sørensen (2017). As expected, the velocity deficits are more pronounced downwind within the wind farm as the second and third rows are waked by upwind turbines. Wakes and velocity deficits depend on the operating turbine's thrust coefficient and are thus strongly dependent on the incoming hub-height wind speed. The velocity deficits for the first row of turbines are dependent on the incoming wind speeds, which are 7.8 m s^{-1} and 11.6 m s^{-1} for the weak and strong stability regimes, respectively. In general, wind turbines (and specifically the turbine used

390 in this study) have higher thrust coefficients at slower wind speeds, which then decrease as the wind speed increases. As a result, the velocity deficit for the first row of turbines in the farm is strongest for the weakly stable regime and weakest for the strongly stable regime. The downwind turbines within the farm have stronger wake deficits compared to the first row for both stability regimes due to the lower wind speed, and thus higher thrust coefficients that these turbines experience.

The vertical structure of the wake deficits persists for over $30D$ downwind and depends strongly on the height of the LLJ.

395 Time-averaged vertical transects of wind speed aligned with the middle of the wind farm are shown in Figs. 10(a) and 10(b) for both stability regimes. The wakes of the turbines are a cumulative effect of individual wind turbine wakes morphing into a wind farm wake, which is consistent with observations of wind farm wakes during SBL conditions (Hirth and Schroeder, 2013). Additionally, these cumulative wakes can adversely affect downwind wind farms (Lundquist et al., 2019). The effect of the wind farm wake is most clear for the strongly stable regime where slower wind speeds above the LLJ nose persist downwind.

400 At altitudes within and below the LLJ, the wake recovers relatively quickly because of the ambient turbulence; however, above the LLJ where turbulence levels are low, the wake recovers extremely slowly. Of course, the altitude of the LLJ, and therefore
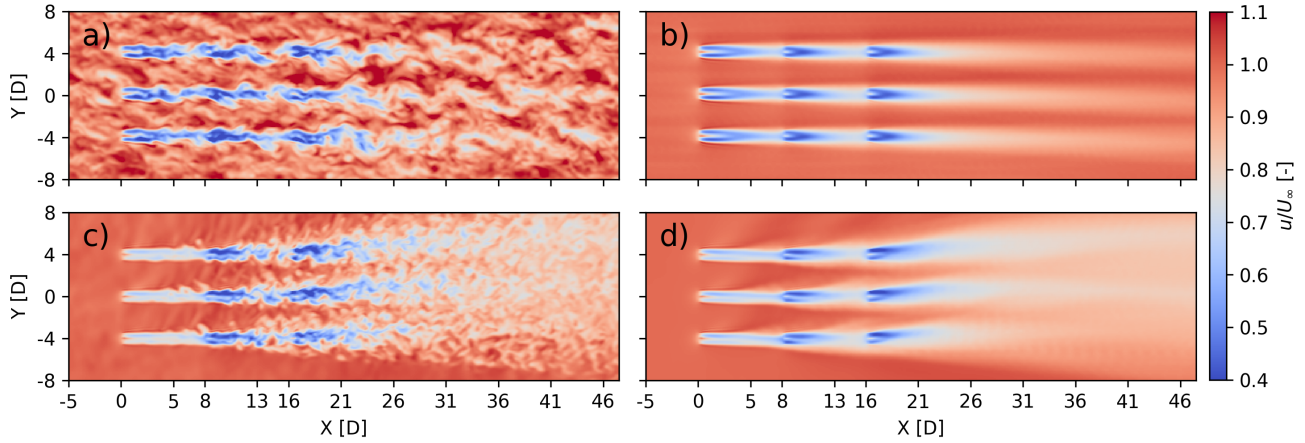
Figure 9. Instantaneous (a,c) and 1-hr time-averaged (b,d) plan view of velocity deficits at hub height for the weakly (a,b) and strongly (c,d) stable regimes.

the wake recovery, is dictated by the stability. The average inflow TKE value at 50 m for the strongly stable regime is 0.086 m^2 s^{-2}, while it is 0.032 m^2 s^{-2} at 80 m and just 0.004 m^2 s^{-2} at 110 m.

The slow recovery of velocities downwind of the farm in the strongly stable regime is also evident in Fig. 10(c), which

405 shows hub-height wind speed normalized by the wind speed at -5D, also with averaging in the spanwise direction to account for the width of the farm. The initial decrease in wind speed after the first row of turbines is greatest at 15% for the weakly stable regime; however, the greatest decrease in wind speed at the end of the farm is for the strongly stable regime where the deficit is 25% after the third row of turbines. These trends are similar to those observed by Gadde and Stevens (Gadde and Stevens, 2021a) who saw that wake deficits for farms that interact with LLJs are greatest when the LLJ height is similar

410 to the hub-height. For the strongly stable case, when the LLJ height is similar to a wind turbine's hub-height, momentum transfer (entrainment) is reduced because the LLJ structure is significantly impacted by the drag of the wind turbine rotors. Any entrainment for this case must come from the slower wind speeds above or below the LLJ. In contrast, for the weakly stable case, entrainment from the faster wind speeds in the LLJ nose above the rotor disk aids in wake recovery.

Intermittent turbulence in the inflow for the strongly stable regime is overpowered by the wake-added turbulence from the

415 wind farm. Figure 11 shows the CDFs of sorted TKE at locations of 5D upwind (x = -5D) and 10D downwind (x = 26D) of the wind farm for both stability regimes at 50 m above the ground. The intermittency fractions for the weakly stable regime is close to 40% while for the strongly stable regime, the intermittency fraction is 29%. As previously mentioned, this means that the strongly stable regime is turbulent only in bursts at this height, while for the weakly stable regime, the turbulence is continuous and nearly uniform. Downwind of the wind farm, the intermittency fraction for both stability regimes is similarly close to

420 40% indicating that wake-added turbulence now drives the distribution of turbulence. Wake-added turbulence is continuous throughout the hour-long period, i.e., without distinct periods of turbulence intermittency. The mean TKE value over the hour-
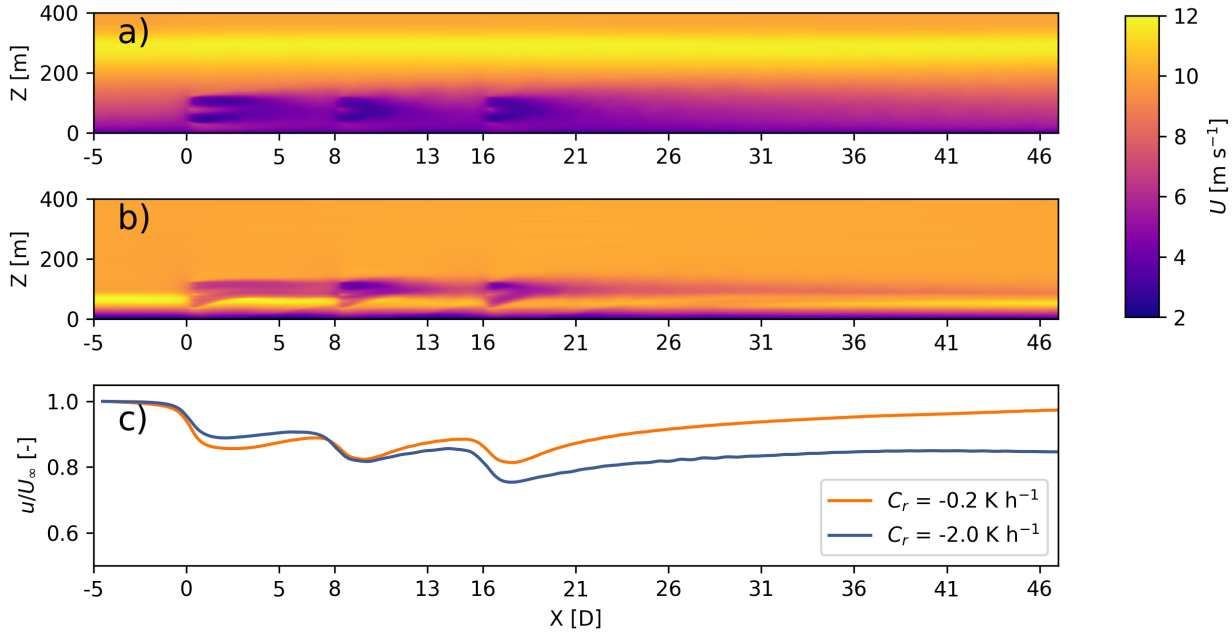
Figure 10. Time-averaged vertical transect of wind speed for the (a) weakly and (b) strongly stable regimes. (c) Hub-height wind speed as a streamwise distance normalized by the wind speed $5D$ upwind of the first row of turbines for each stability regime. For (c), the wind speed is averaged in the spanwise direction (-$5D$ to $5D$) to account for the three turbines in each row within the wind farm.

long period at this height for the strongly stable case is 0.09 m^2 s^{-2} upwind of the farm, while it is 0.40 m^2 s^{-2} $10D$ downwind of the farm. Therefore, ambient turbulence is minimal compared to contributions from the wake in the strongly stable regime.

The added TKE from the farm impacts the SBL in a number of ways. Figures 12(a) and 12(b) show wind speed and
425 momentum flux averaged across the spanwise transects in Fig. 1 at $5D$ upwind (x = -$5D$) and $5D$ downwind of the farm (x = $21D$) for both stability regimes. The momentum flux is normalized by the value at the surface for each individual case. For both regimes, the velocity deficit due to the wind farm wake is evident in reduced velocities within the rotor layer. The wind speeds are also decreased above the rotor layer because momentum is entrained into the wake from above, as indicated by negative momentum flux values in Fig. 12(b). For the strongly stable regime, the momentum flux is mostly positive in the
430 bottom half of the rotor disk indicating that momentum is transferred from below, and this is because the nose of the LLJ is slightly below hub-height and the upper half of the rotor disk is in the negative shear region. This entrainment from below that aids in wake recovery agrees with modeling results from other work (Gadde and Stevens, 2021b).

The wakes also affect the thermodynamic characteristics of the stable layers. The spanwise averaged potential temperature and heat flux are shown in Figs. 12(c) and 12(d), respectively. The depth of the stable layer increases and the temperature
435 gradient is reduced across the rotor disk most prominently for the strongly stable regime. For both stability regimes, the heat flux is negative throughout the vertical profile indicating that warmer air is entrained from above. The wind farm induced
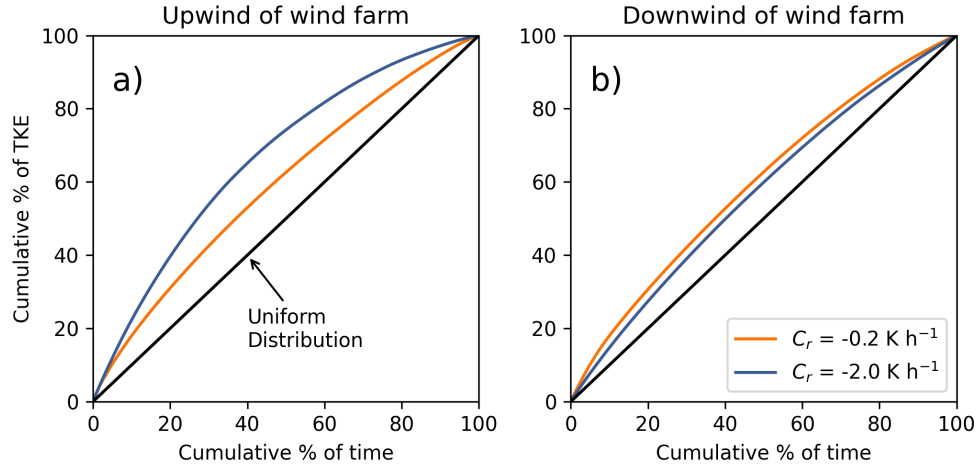
Figure 11. Cumulative distribution function of TKE (a) $5D$ upwind (x = -5D) and (b) $10D$ downwind (x = 26D) of the wind farm for each stability regime at z = 50 m.

change in stratification is also visible in Fig. 13, which shows the spanwise averaged change in temperature (compared to -5D) as a function of height at various streamwise locations. For the strongly stable regime, the temperature decreases in the upper half of the rotor disk and increases in the lower half of the rotor disk. Similar trends hold for the weakly stable regimes but

440   centered around the top of the rotor disk, although the changes in temperature are much smaller for the weakly stable regime. The wind farm, in effect, creates a less stable layer from the ground to the top of the rotor disk and even up to 80 m above the rotor disk for the weakly stable regime. These wind farm induced effects on the SBL persist over $30D$ downwind of the farm.

3.4   Effect of intermittent turbulence on farm performance

Considering the intermittent turbulence present in the strongly stable regime, the following work aims to to understand and

445   quantify how intermittency affects wind turbine wake recovery as well as power production. To examine the flow structure during turbulent and quiescent periods for the strongly stable regime, we look at plan slices of the velocity deficit and TKE at 50 m above the ground. Figures 14(a) and 14(c) show a quiescent instance of velocity deficit and TKE while Figs. 14(b) and 14(d) show a turbulent instance. Note that the colorbar in Figs. 14(c) and 14(d) is truncated at a maximum value of 2.0 m^2 s^{-2} so that the inflow turbulence is more pronounced; there are higher values downwind due to wake-added turbulence which

450   are not apparent with this colorbar. For the turbulent instance, smaller coherent structures are visible in the velocity deficits upwind of the first row of turbines as well as between the first and second row of turbines. These structures represent coherent turbulent eddies and are evident in the plan slice of TKE in Fig. 14(d).

    The TKE is up to 10 times higher during turbulent periods compared to quiescent periods. However, the turbulent periods have little effect on wake recovery as downwind of the turbines, turbulence is largely wake-generated. Figure 15 shows the

455   spanwise averaged (-5D to 5D) velocity deficit profiles within the wind farm and downwind of the wind farm. The veloc-
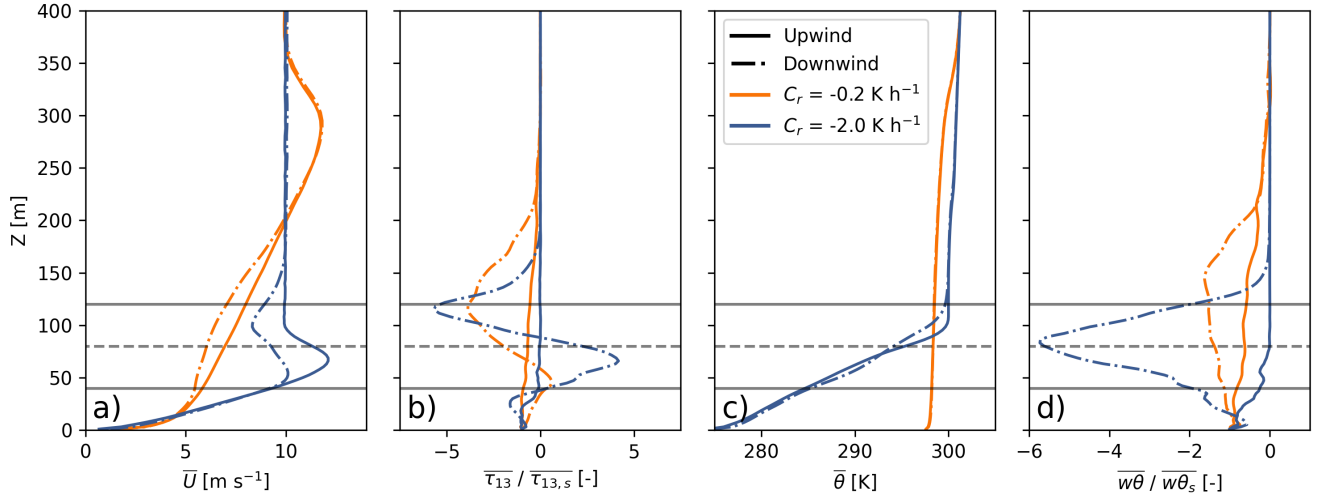
Figure 12. Vertical profiles of (a) wind speed, (b) streamwise vertical momentum flux, (c) potential temperature, and (d) vertical heat flux, $5D$ upwind (x = -5D) and $5D$ downwind (x = 21D) of the farm for each stability regime. The solid horizontal lines represent the bottom and top of the rotor layer while the dashed line represents hub-height.
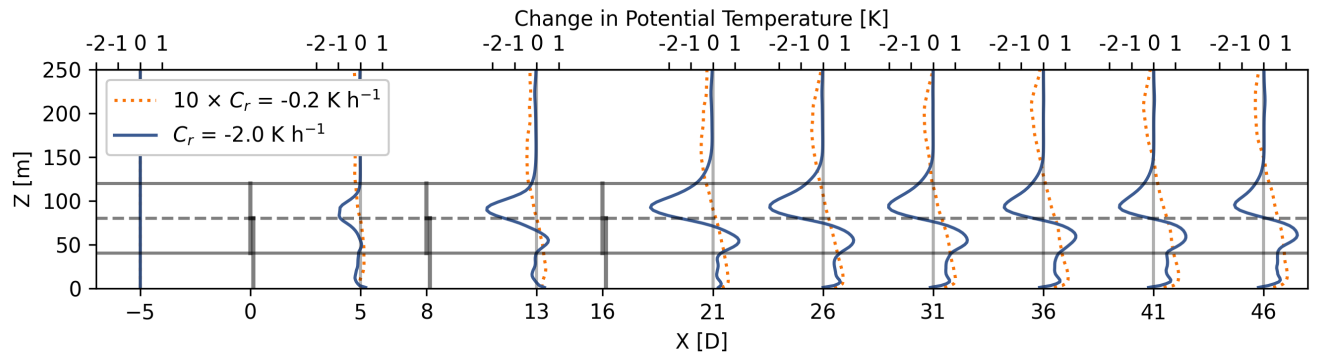
Figure 13. Spanwise averaged profiles for the change in potential temperature at various distances (relative to x = -5D) for each stability regime. Note that the profiles for the weakly stable regime have been amplified by a factor of 10 for visualization purposes. The solid horizontal lines represent the bottom and top of the rotor layer while the dashed line represents hub-height.
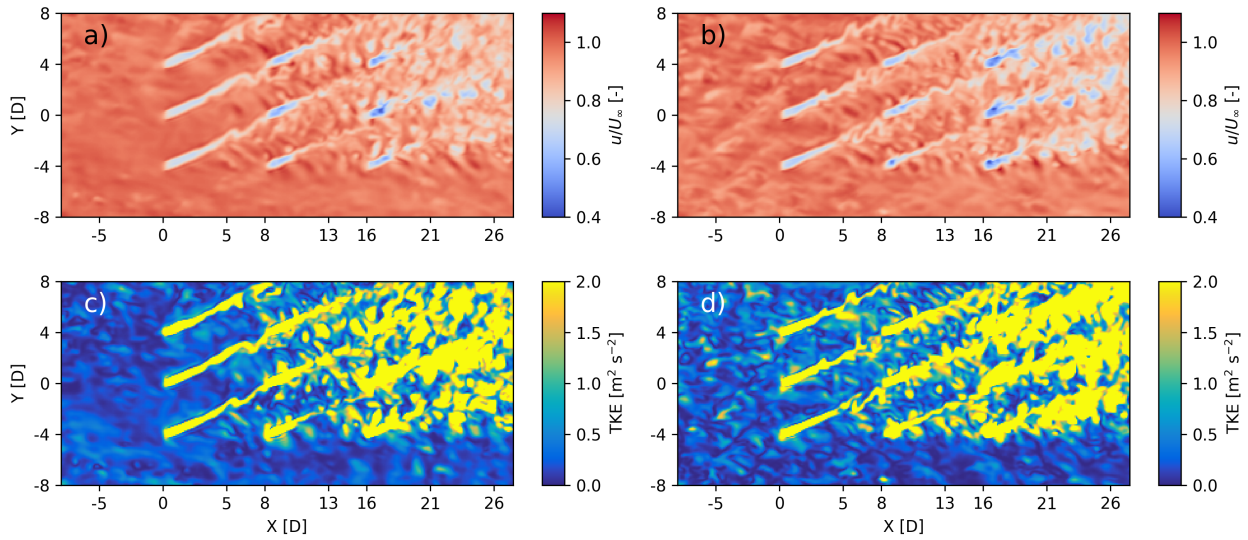
Figure 14. Example (a,c) quiescent and (b,d) turbulent instantaneous plan view of (a,b) velocity deficits and (c,d) TKE at 50 m above the ground for the strongly stable regime.
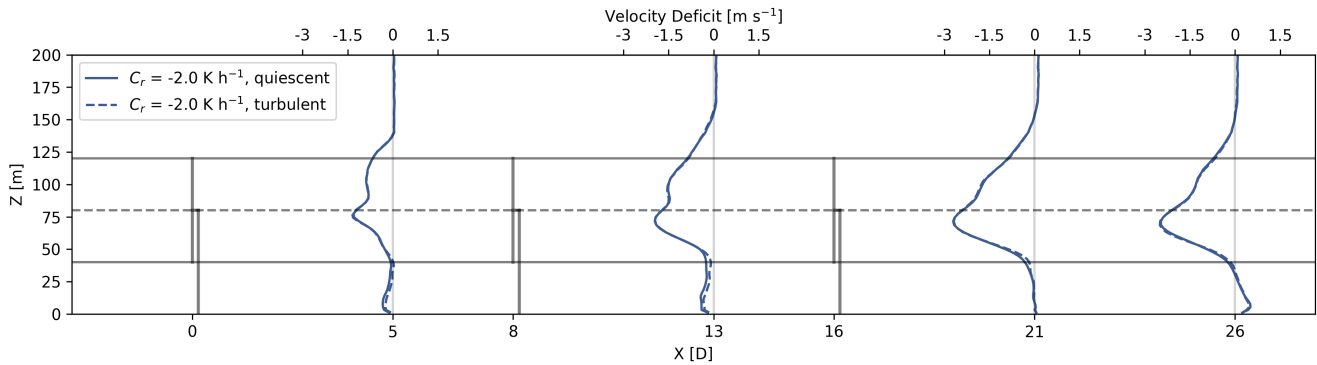
Figure 15. Velocity deficit profiles at various streamwise locations (relative to x = -5D) separated by quiescent and turbulent periods for the strongly stable regime. The solid horizontal lines represent the bottom and top of the rotor layer while the dashed line represents hub-height.

ity deficit profiles have been separated by whether the flow is more turbulent or quiescent using the procedure described in Sec. 3.2. The velocity deficits are nearly identical regardless of the streamwise location. This is because, while the TKE is much larger during turbulent periods compared to quiescent periods, the TKE during the turbulent periods is still very small when compared to the weak stability regime or to the wake-added turbulence from the wind turbines. The larger turbulence during the intermittent turbulence does not aid in wake-mixing since turbulence levels are so small and thus, the velocity deficits are only marginally impacted as seen by the solid and dashed lines nearly overlapping in Fig. 15.

460
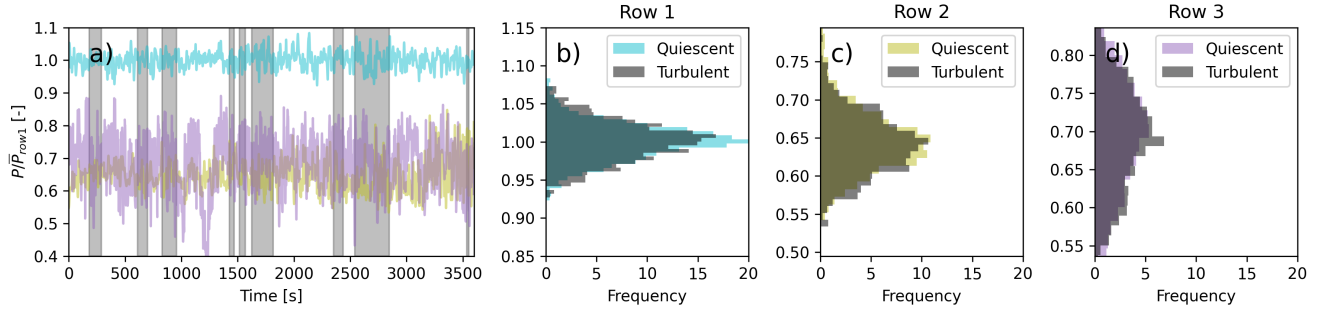
Figure 16. Time-series (a) and histograms by row (b,c,d) of detrended power normalized by the rated power of the turbine for the strongly stable regime. The periods highlighted in gray are turbulent while periods in white are quiescent, as determined by the method in Sec. 3.2.

The intermittent turbulence resolved in this study does not significantly affect the average power production but does have a small effect on the power variability of the wind farm during the strongly stable regime. Figure 16(a) shows the time-series of the average power production during the analysis period for each row of turbines within the farm, normalized by the rated

465 power, with turbulent periods highlighted in gray. Figures 16(b), 16(c), and 16(d) show histograms of the power production to provide insight into the spread for each row. Note that the turbine used in this study can produce power greater than its rated power [greater than 1 in Fig. 16(a)] for wind speeds in the range of 10-13 m s^{-1} as discussed in Arthur et al. (2020), which impacts the distribution of the power signal. The first row sees the largest difference in variability with the standard deviation being 45.7 kW during turbulent periods and 40.8 kW during quiescent periods or a roughly 13% increase in the

470 power variability. Regarding average power, the front row performance is largely unchanged during quiescent and turbulent periods (1712 kW vs 1713 kW) as differences in the mean wind speeds are very small for the different periods. For the second and third rows, average power and power variability are largely independent of intermittent turbulence for the same reasons as described above (their inflow is dominated by characteristics of upwind wakes).

4 Conclusions

475 In this study, the WRF-LES-GAD framework is used to provide insight into how wind farms interact with weakly and strongly stable atmospheric boundary layer conditions. The primary focus is to determine 1) how the presence of wind turbine wakes affects stable boundary layer evolution, and 2) how the intermittent turbulence in strongly stable boundary layers affects power production and wake recovery. A one-way nested approach is used with idealized LES, where turbulence is spun-up on the outer domain using doubly periodic lateral boundary conditions. The outer domain provided forcing for the inner domain

480 containing a 3 × 3 wind farm consisting of nine 1.6-MW turbines. The grid spacing was the same in each domain, meaning that the fully-developed turbulent structures from the periodic outer domain are passed directly into the inner domain.

The explicit filtering framework and dynamic reconstruction turbulence model of Chow et al. (2005) is used to extend the working range of LES in the stable boundary layer and, as a result, turbine-airflow interactions can be studied in such strongly

stable conditions with realistic turbulence. The development of the boundary layer on the outer domain was first compared
485 between the DRM closure and the commonly used TKE-1.5 closure. The percentage of vertically integrated resolved heat
flux of the total heat flux was similar across both closures at a relatively coarse, 8 m horizontal resolution for the weakly
stable regime. However, for the strongly stable regime, the DRM closure resolved a larger fraction of the heat flux compared
to the TKE-1.5 closure, indicating improved representation of heat flux (and, by extension, other turbulence quantities) in the
resolved flow field. The TKE-1.5 closure is entirely dissipative by nature, while the DRM closure is able to physically represent
490 the backscatter of turbulence from smaller scales to larger scales, which was shown to be especially important as it relates to
the momentum flux in strongly stable boundary layers.

For both stability conditions, a low-level jet formed at the top of the stable layer with the height of the jet relative to the
turbine having a major impact on the SBL evolution downwind. The height of this jet decreased with increasing stability,
with the jet being above the rotor disk for the weakly stable regime and just below hub-height for the strongly stable regime.
495 Below the LLJ, continuous turbulence formed in the weakly stable regime, but turbulence occurred intermittently (in addition
to background turbulence) for the strongly stable regime due to a balance between shear-generated turbulence and buoyancy
suppression. The wind farm in the strongly stable regime experienced intermittent turbulence below hub-height (50% of the
turbulence occurs in just 29% of the simulation time) and very little turbulence along with a negative wind shear region in the
upper half of the rotor disk. Downwind of the wind farm, turbulence was no longer intermittent as the flow structures were
500 dominated by continuous, wake-added turbulence. Additionally, momentum transfer was dependent on the altitude of the LLJ.
For the strongly stable regime, momentum was largely transferred upwards from the LLJ below hub-height to aid in wake
recovery, whereas for the weakly stable regime, momentum was entrained from higher wind speeds within the LLJ aloft. Heat
was always transferred downward from above for both stability regimes, resulting in a less stable layer downwind of the farm.

For the strongly stable regime, periods of elevated intermittent turbulence increased wind farm power variability but had
505 little impact on the average power production. The standard deviation in the power output for the first row of turbines within
the farm was 13% higher during turbulent periods compared to quiescent periods. However, downwind rows were not affected
by this power variability because the turbulence the downwind turbines experience was wake-added and thus more continuous.
The focus of this study was on turbine power production; the impact of intermittent turbulence on structural loading is an
avenue for future work.

510 Both the numerical methods and analyses used in this idealized study can be extended to the conditions observed during
AWAKEN or other future field campaigns. In particular, the DRM closure provides a less computationally expensive frame-
work for modeling the SBL and interaction with wind farms. Recently, the DRM closure has also been used in multi-scale
WRF-LES-GAD simulations for AWAKEN, with realistic time-varying inflow conditions downscaled from reanalysis data
while also incorporating topography (Wise et al., 2025). The intermittent turbulence explored in this study is a result of the
515 competition between shear production and buoyancy suppression. Other mechanisms for SBL intermittency that are common
in the U.S. Southern Great Plains, the region for the AWAKEN field campaign, include breaking gravity waves, bores, Kelvin-
Helmholtz billows, terrain-induced flows, and propagating density currents. While the intermittent turbulence simulated as part
of this study had only a modest impact on wind farm performance, Wise et al. (2025) showed that another type of intermittent

turbulence (gravity waves in their case) can result in significant impacts on average power production and the power variability. Ultimately, this study demonstrated a methodology for identifying and quantifying intermittent turbulence events from a time-series of TKE. These methods can be used in future work with observations from meteorological towers, vertical profiling lidars, and supervisory control and data acquisition (SCADA) data from AWAKEN to examine wind farm performance in various intermittent turbulence conditions.

Code and data availability. The data that support the findings of this study are available from the corresponding author upon reasonable request. The WRF source code that support the findings of this study are openly available: https://github.com/adamwise95/WRFv4.4-DRM_ GAD.

Appendix A: Turbulence representation on different grids for the TKE-1.5 and DRM closures

The resolved and modeled heat fluxes can be used as a proxy to determine the percentage or fraction of resolved turbulence. This is done by calculating the vertically integrated resolved heat flux (q) divided by the vertically integrated total heat flux

530   (Q). This quantity provides insight into whether the turbulence closure needs to model turbulence or if it can be resolved in the LES. For the DRM closure, the total heat flux includes the resolved component as well as the RSFS and SGS terms. For TKE-1.5, the total heat flux includes the resolved component and SGS term. Table A1 shows the percentage of resolved heat flux for both stability regimes and at horizontal grid spacings of 8 m and 4 m.

For all the resolutions and both turbulence closures, the percentage of resolved heat flux to total heat flux decreases with

535   increasing stratification. This indicates that runaway cooling does not occur in any of the simulations (Jiménez and Cuxart, 2005; Zhou and Chow, 2011). At 8 m resolution and for the strongly stable case, the DRM closure resolves over 30% of the heat flux, while the TKE-1.5 closure resolves just 11%. Even though the two closures have comparable average surface heat flux values during the analysis period (-0.041 K m s^{-1} for the TKE-1.5 closure and -0.040 K m s^{-1} for the DRM closure), the quality of resolved turbulence is substantially different. The DRM closure resolves nearly three times as much turbulence on

540   this grid for the strongly stable regime compared to the TKE-1.5 closure and, as a result, simulates more realistic turbulence. For the weakly stable regime, the DRM and TKE-1.5 closures perform comparably. When the grid resolution is increased, both closures resolve more of the heat flux but with greater improvement for the TKE-1.5 closure versus the DRM closure. The TKE-1.5 closure is improved significantly for the strongly stable case when the grid spacing decreases to 4 m and resolves a similar but slightly lower percentage of the heat flux at 26% vs 32% for the DRM closure. Additionally, for the weakly stable

545   case [Fig. 3(a)], the TKE-1.5 closure resolves more heat flux. This is because, for the DRM closure, the effect of incorporating explicit filtering increases the total SFS modeled stress and thus the resolved stress must decrease accordingly. This is a known feature of the DRM which helps decrease numerical error near the filter cutoff. For the strongly stable regime [Fig. 3(c)], much of the heat flux is modeled so the effect of the RSFS term on the resolved field is less pronounced. Similar results to the q/Q ratios hold for other turbulence quantities such as turbulent kinetic energy (TKE) or momentum flux (not shown).

550   The computational cost factor in Table A1 is calculated by comparing the wall-clock time each simulation takes relative to the 8 m, weakly stable simulation using the TKE-1.5 closure. The cost factor inherently accounts for the decrease in time step required when the grid resolution is increased. The time steps used are 0.5 s and 0.2 s, for the 8 m and 4 m grid spacing simulations, respectively. The same number of grid points is used for the 4 m configuration due to computational expense, as four times the number of grid points would be needed to keep the domain size consistent. The vertical resolution for the 8 m

555   and 4 m configurations are identical (as defined previously). The cost factor is also adjusted to compare a constant physical domain size when the grid resolution is increased, which results in a default factor of 4 in the cost calculation for the 4 m grid spacing simulations compared to the 8 m case. For example, on 400 processors, the 8 m grid spacing TKE-1.5 weakly stable simulation takes 4.1 hrs of real-time for every 1 hr of simulation time. While the configuration with 4 m grid spacing takes 10.0 hrs with the same number of grid points. When the factor of 4 is included to compare a constant physical domain size, the

560   4 m grid spacing simulation would take 40.2 hrs, which results in a computational cost factor of 9.72. Using the DRM closure

Table A1. Vertically integrated resolved heat flux q over total (resolved + subfilter) heat flux Q and computational cost factor for the TKE-1.5 and DRM closures at various horizontal grid spacings. The computational cost factor is the increase in computation cost relative to the 8 m, weakly stable simulation using the TKE-1.5 closure.

Cooling Rate ($K\,h^{-1}$)	Grid Spacing (m)	q/Q (%)	Computational Cost Factor
Closure: TKE-1.5			
-0.2	8	75.1	1.00
-2.0	8	11.2	0.99
-0.2	4	85.0	9.72
-2.0	4	26.1	10.67
Closure: DRM			
-0.2	8	66.7	1.45
-2.0	8	32.4	1.46
-0.2	4	72.7	13.22
-2.0	4	32.4	13.39

at the same resolution as the TKE-1.5 closure is 1.45 times the computational cost. At the same resolution, the TKE-1.5 closure outperforms the DRM closure with respect to q/Q for the weakly stable regime at less computational cost. However, the DRM closure outperforms the TKE-1.5 closure for the strongly stable case even at the coarser 8 m grid spacing compared to the 4 m TKE-1.5 configuration, although the differences in q/Q are minor. For the strongly stable case, the TKE-1.5 closure at 4 m

565   resolution will resolve similar levels of turbulence at 7.3 times (10.67/1.46 from Table A1) the computational cost compared to the DRM closure at 8 m resolution. As a result, the DRM closure is better suited and more computationally efficient than the TKE-1.5 closure for simulating strongly stable boundary layers at coarser grid spacings. There are additional benefits of the DRM closure in the representation of intermittent turbulence, as further described in the main text of this paper. Note that there are some differences in the computational cost factor for the same resolution and closure, but with different cooling rates

570   because the cost can vary slightly in the MOST iterative procedure at the surface.

Lastly, plan views of TKE at 50 m above the ground (70% of the boundary layer height) for the TKE-1.5 closure at 8 m and 4 m grid spacings are shown in Fig. A1. The TKE signals are processed in a similar manner as those shown for the DRM closure in Fig. 8. At 8 m grid spacing, the TKE signal displays wave-like patterns that are numerical artifacts due to unphysical temperature gradients. When using the TKE-1.5 closure, only by reducing the horizontal grid spacing from 8 m to 4 m does

575   the turbulence exhibit similar characteristics to the DRM closure at a horizontal grid spacing of 8 m. This is expected for the strongly stable regime as using the DRM closure at 8 m horizontal grid spacing resolves a similar level of heat flux (a proxy for TKE) as using the TKE-1.5 closure at 4 m horizontal grid spacing (Table A1).
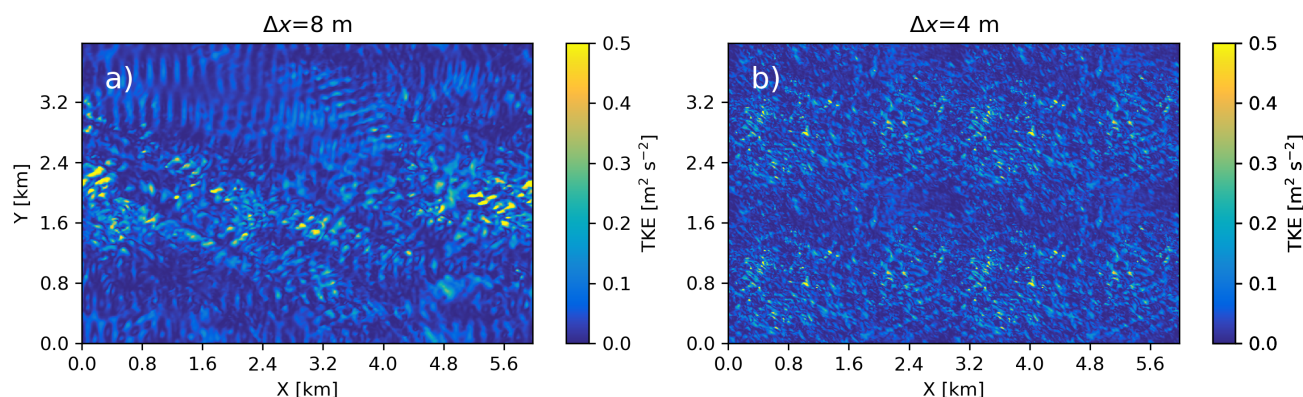
Figure A1. Instantaneous plan view of TKE at the beginning of the analysis period at 50 m above the ground for the strongly stable regime using the TKE-1.5 closure at (a) 8 m horizontal grid spacing and (b) 4 m horizontal grid spacing. Note that the domain is tiled in (b) for visualization purposes as the simulated domain for the 4 m grid spacing case is half of the length and width compared to the 8 m grid spacing case. Evident in (a) are wave-like patterns that are numerical artifacts.

Author contributions. Writing—original draft preparation and visualization, ASW; writing—review and editing, RSA, JDM, JKL, and FKC; methodology, software, validation, and formal analysis, ASW, RSA, and JDM; conceptualization, ASW and FKC. All authors contributed
580 with critical feedback on this research and have read and agreed to the published version of the manuscript.

Competing interests. At least one of the (co-)authors is a member of the editorial board of *Wind Energy Science*.

Acknowledgements. The authors would like to acknowledge Xiaoming Shi of the Hong Kong University of Science and Technology for leading the efforts in moving the DRM closure from WRFv3 to WRFv4. Correspondence with Jason Simon of the University of New Hampshire regarding the DRM code structure was greatly appreciated. We would also like to acknowledge discussions with Peter Sullivan of
585 the National Center of Atmospheric Research regarding the many definitions of intermittent turbulence and on the interplay of intermittency with backscatter. This material is based upon work by ASW supported by the National Science Foundation Graduate Research Fellowship Program under Grant No. DGE 1752814. This research used the Savio computational cluster resource provided by the Berkeley Research Computing program at the University of California, Berkeley (supported by the UC Berkeley Chancellor, Vice Chancellor for Research, and Chief Information Officer). The authors are grateful for support from Sandia National Laboratories as part of the AWAKEN project. RSA's
590 and JDM's contributions were prepared by Lawrence Livermore National Laboratory under Contract DE-AC52-07NA27344, with support from the U.S. DOE Office of Energy Efficiency and Renewable Energy Wind Energy Technologies Office. This work was authored [in part] by the National Renewable Energy Laboratory, operated by Alliance for Sustainable Energy, LLC, for the U.S. Department of Energy (DOE) under Contract No. DE-AC36-08GO28308. Funding provided by the U.S. Department of Energy Office of Energy Efficiency and Renewable Energy Wind Energy Technologies Office. The views expressed in the article do not necessarily represent the views of the DOE
595 or the U.S. Government. The U.S. Government retains and the publisher, by accepting the article for publication, acknowledges that the U.S.

References

Ansorge, C. and Mellado, J. P.: Global intermittency and collapsing turbulence in the stratified planetary boundary layer, Bound.-Layer
600   Meteor., 153, 89–116, 2014.

Ansorge, C. and Mellado, J. P.: Analyses of external and global intermittency in the logarithmic layer of Ekman flow, J. Fluid Mech., 805,
611–635, 2016.

Arthur, R. S., Mirocha, J. D., Marjanovic, N., Hirth, B. D., Schroeder, J. L., Wharton, S., and Chow, F. K.: Multi-Scale Simulation of Wind
Farm Performance during a Frontal Passage, Atmosphere, 11, 245, https://doi.org/10.3390/atmos11030245, 2020.

605 Banta, R. M.: Stable-boundary-layer regimes from the perspective of the low-level jet, Acta Geophysica, 56, 58–87,
https://doi.org/10.2478/s11600-007-0049-8, 2008.

Bardina, J., Ferziger, J., and Reynolds, W.: Improved Turbulence Models Based on Large Eddy Simulation of Homgeneous, Imcompressible,
Turbulent Flows., Tech. rep., Stanford University, 1983.

Beare, R. J., Macvean, M. K., Holtslag, A. A. M., Cuxart, J., Esau, I., Golaz, J.-C., Jimenez, M. A., Khairoutdinov, M., Kosovic, B., Lewellen,
610   D., Lund, T. S., Lundquist, J. K., Mccabe, A., Moene, A. F., Noh, Y., Raasch, S., and Sullivan, P.: An Intercomparison of Large-Eddy
Simulations of the Stable Boundary Layer, Boundary-Layer Meteorology, 118, 247–272, https://doi.org/10.1007/s10546-004-2820-6,
2006.

Brown, A. R., Hobson, J. M., and Wood, N.: Large-Eddy Simulation Of Neutral Turbulent Flow Over Rough Sinusoidal Ridges, Boundary-
Layer Meteorology, 98, 411–441, https://doi.org/10.1023/A:1018703209408, 2001.

615 Businger, J. A., Wyngaard, J. C., Izumi, Y., and Bradley, E. F.: Flux-Profile Relationships in the Atmospheric Surface Layer, Journal of
Atmospheric Sciences, 28, 181 – 189, https://doi.org/10.1175/1520-0469(1971)028<0181:FPRITA>2.0.CO;2, 1971.

Carper, M. A. and Porté-Agel, F.: The role of coherent structures in subfilter-scale dissipation of turbulence measured in the atmospheric
surface layer, Journal of Turbulence, 5, N40, https://doi.org/10.1088/1468-5248/5/1/040, 2004.

Chow, F. K., Street, R. L., Xue, M., and Ferziger, J. H.: Explicit Filtering and Reconstruction Turbulence Modeling for Large-Eddy Simulation
620   of Neutral Boundary Layer Flow, Journal of the Atmospheric Sciences, 62, 2058–2077, https://doi.org/10.1175/JAS3456.1, 2005.

Coulter, R. and Doran, J.: Spatial and Temporal Occurrences of Intermittent Turbulence During CASES-99, Boundary layer Meteorology,
105, 329–349, https://doi.org/10.1023/A:1019993703820, 2002.

Deardorff, J. W.: Stratocumulus-capped mixed layers derived from a three-dimensional model, Boundary-Layer Meteorology, 18, 495–527,
1980.

625 Ellison, A. M.: EFFECT OF SEED DIMORPHISM ON THE DENSITY-DEPENDENT DYNAMICS OF EXPERIMENTAL
POPULATIONS OF ATRIPLEX TRIANGULARIS (CHENOPODIACEAE), American Journal of Botany, 74, 1280–1288,
https://doi.org/https://doi.org/10.1002/j.1537-2197.1987.tb08741.x, 1987.

Gadde, S. N. and Stevens, R. J. A. M.: Effect of low-level jet height on wind farm performance, Journal of Renewable and Sustainable
Energy, 13, 013 305, https://doi.org/10.1063/5.0026232, 2021a.

630 Gadde, S. N. and Stevens, R. J. A. M.: Interaction between low-level jets and wind farms in a stable atmospheric boundary layer, Physical
Review Fluids, 6, 014 603, https://doi.org/10.1103/PhysRevFluids.6.014603, 2021b.

Hirth, B. and Schroeder, J.: Documenting Wind Speed and Power Deficits behind a Utility-Scale Wind Turbine, Journal of Applied Meteo-
rology and Climatology, 52, 39–46, https://doi.org/10.1175/JAMC-D-12-0145.1, 2013.

Holtslag, A. A. M. and Nieuwstadt, F. T. M.: Scaling the atmospheric boundary layer, Boundary-Layer Meteorology, 36, 201–209, https://doi.org/10.1007/BF00117468, 1986.

Jiménez, M. A. and Cuxart, J.: Large-Eddy Simulations of the Stable Boundary Layer Using the Standard Kolmogorov Theory: Range of Applicability, Boundary-Layer Meteorology, 115, 241–261, https://doi.org/10.1007/s10546-004-3470-4, 2005.

Kelley, N., Jonkman, B., and Scott, G.: Great Plains Turbulence Environment: Its Origins, Impact, and Simulation, 2006.

Kirkil, G., Mirocha, J., Bou-Zeid, E., Chow, F. K., and Kosović, B.: Implementation and Evaluation of Dynamic Subfilter-Scale Stress Models for Large-Eddy Simulation Using WRF*, Monthly Weather Review, 140, 266–284, https://doi.org/10.1175/MWR-D-11-00037.1, 2012.

Kosović, B.: Subgrid-scale modelling for the large-eddy simulation of high-Reynolds-number boundary layers, Journal of Fluid Mechanics, 336, 151–182, https://doi.org/10.1017/S0022112096004697, 1997.

Krishnamurthy, R., Newsom, R. K., Chand, D., and Shaw, W. J.: Boundary Layer Climatology at ARM Southern Great Plains, https://doi.org/10.2172/1778833, 2021.

Lilly, D. K.: A proposed modification of the Germano subgrid-scale closure method, Physics of Fluids A: Fluid Dynamics, 4, 633–635, https://doi.org/10.1063/1.858280, 1992.

Lu, H. and Porté-Agel, F.: Large-eddy simulation of a very large wind farm in a stable atmospheric boundary layer, Physics of Fluids, 23, 065 101, https://doi.org/10.1063/1.3589857, 2011.

Lundquist, J. K., DuVivier, K. K., Kaffine, D., and Tomaszewski, J. M.: Costs and consequences of wind turbine wake effects arising from uncoordinated wind energy development, Nature Energy, 4, 26–34, https://doi.org/10.1038/s41560-018-0281-2, 2019.

Mahrt, L.: Vertical Structure and Turbulence in the Very Stable Boundary Layer, Journal of Atmospheric Sciences, 42, 2333 – 2349, https://doi.org/10.1175/1520-0469(1985)042<2333:VSATIT>2.0.CO;2, 1985.

Mahrt, L.: Intermittency of Atmospheric Turbulence, Journal of Atmospheric Sciences, 46, 79 – 95, https://doi.org/10.1175/1520-0469(1989)046<0079:IOAT>2.0.CO;2, 1989.

Mahrt, L.: Stratified Atmospheric Boundary Layers, Boundary-Layer Meteorology, 90, 375–396, https://doi.org/10.1023/A:1001765727956, 1999.

Mahrt, L.: Stably Stratified Atmospheric Boundary Layers, Annual Review of Fluid Mechanics, 46, 23–45, https://doi.org/https://doi.org/10.1146/annurev-fluid-010313-141354, 2014.

Marjanovic, N., Mirocha, J. D., Kosović, B., Lundquist, J. K., and Chow, F. K.: Implementation of a generalized actuator line model for wind turbine parameterization in the Weather Research and Forecasting model, Journal of Renewable and Sustainable Energy, 9, 063 308, https://doi.org/10.1063/1.4989443, 2017.

Mason, P. J. and Thomson, D. J.: Stochastic backscatter in large-eddy simulations of boundary layers, Journal of Fluid Mechanics, 242, 51–78, https://doi.org/10.1017/S0022112092002271, 1992.

Mayor, S. D., Jachens, E. R., and Randall, T. N.: Lidar observations of fine-scale gravity waves in the nocturnal boundary layer above an orchard canopy, in: 16th International Symposium for the Advancement of Boundary-Layer Remote Sensing (ISARS), CIRES, University of Colorado and NOAA Earth System Research Laboratory, Boulder, CO, 2012.

Mirocha, J., Kosović, B., and Kirkil, G.: Resolved Turbulence Characteristics in Large-Eddy Simulations Nested within Mesoscale Simulations Using the Weather Research and Forecasting Model, Monthly Weather Review, 142, 806–831, https://doi.org/10.1175/MWR-D-13-00064.1, 2014a.

670   Mirocha, J. D., Kosović, B., Aitken, M. L., and Lundquist, J. K.: Implementation of a generalized actuator disk wind turbine model into the weather research and forecasting model for large-eddy simulation applications, Journal of Renewable and Sustainable Energy, 6, 013 104, https://doi.org/10.1063/1.4861061, 2014b.

Mirocha, J. D., Rajewski, D. A., Marjanovic, N., Lundquist, J. K., Kosović, B., Draxl, C., and Churchfield, M. J.: Investigating wind turbine impacts on near-wake flow using profiling lidar data and large-eddy simulations with an actuator disk model, Journal of Renewable and

675   Sustainable Energy, 7, 043 143, https://doi.org/10.1063/1.4928873, 2015.

Monin, A. S. and Obukhov, A. M.: Basic laws of turbulent mixing in the surface layer of the atmosphere, Contrib. Geophys. Inst. Acad. Sci. USSR, 151, e187, 1954.

Moriarty, P., Hamilton, N., Debnath, M., Herges, T., Isom, B., Lundquist, J., Maniaci, D., Naughton, B., Pauly, R., Roadman, J., Shaw, W., van Dam, J., and Wharton, S.: American WAKE experimeNt (AWAKEN), Tech. Rep. NREL/TP-5000-75789, 1659798, MainId:5894,

680   https://doi.org/10.2172/1659798, 2020.

Moriarty, P., Abraham, A., Bodini, N., Goldberger, L., Hamilton, N., Hirth, B., Iungo, G. V., Jordan, A. M., Kaul, C. M., Letizia, S., Lundquist, J. K., Moss, C., Pichugina, Y., Radünz, W. C., Vöhringer, A. L., Voss, A., Wise, A. S., Bärfuss, K. B., Barthelmie, R. J., Pryor, S. C., Canadillas, B., Cheung, L., Chow, F. K., Frère, A., Herges, T., Krishnamurthy, R., Klein, P. M., Lampert, A., Puccioni, M., Roy, S., Shams Solari, M., Sanchez-Gomez, M., Scholbrock, A., Shartzer, S., Smith, E. N., Turner, D. D., and Wharton, S.: Wind Farm

685   Atmosphere Interactions as seen in the American WAKE ExperimeNt (AWAKEN), Submitted to Bulletin of the American Meteorological Society, 2025.

Optis, M., Monahan, A., and Bosveld, F. C.: Moving Beyond Monin–Obukhov Similarity Theory in Modelling Wind-Speed Profiles in the Lower Atmospheric Boundary Layer under Stable Stratification, Boundary-Layer Meteorology, 153, 497–514, https://doi.org/10.1007/s10546-014-9953-z, 2014.

690   Peña, A., Kosović, B., and Mirocha, J. D.: Evaluation of idealized large-eddy simulations performed with the Weather Research and Forecasting model using turbulence measurements from a 250 m meteorological mast, Wind Energy Science, 6, 645–661, https://doi.org/10.5194/wes-6-645-2021, 2021.

Rottman, J. W. and Simpson, J. E.: The formation of internal bores in the atmosphere: A laboratory model, Quarterly Journal of the Royal Meteorological Society, 115, 941–963, https://doi.org/10.1002/qj.49711548809, 1989.

695   Sanchez Gomez, M., Lundquist, J. K., Mirocha, J. D., Arthur, R. S., Muñoz-Esparza, D., and Robey, R.: Can lidars assess wind plant blockage in simple terrain? A WRF-LES study, Journal of Renewable and Sustainable Energy, 14, 063 303, https://doi.org/10.1063/5.0103668, 2022.

Sanchez Gomez, M., Lundquist, J. K., Mirocha, J. D., and Arthur, R. S.: Investigating the physical mechanisms that modify wind plant blockage in stable boundary layers, Wind Energy Science, 8, 1049–1069, https://doi.org/10.5194/wes-8-1049-2023, 2023.

700   Simon, J. S., Zhou, B., Mirocha, J. D., and Chow, F. K.: Explicit Filtering and Reconstruction to Reduce Grid Dependence in Convective Boundary Layer Simulations Using WRF-LES, Monthly Weather Review, 147, 1805 – 1821, https://doi.org/10.1175/MWR-D-18-0205.1, 2019.

Sisterson, D. L. and Frenzen, P.: Nocturnal boundary-layer wind maxima and the problem of wind power assessment., Environmental Science & Technology, 12, 218–221, https://doi.org/10.1021/es60138a014, 1978.

705   Skamarock, W. C., Klemp, J. B., Dudhia, J., Gill, D. O., Liu, Z., Berner, J., Wang, W., Powers, J. G., Duda, M. G., Barker, D. M., and Huang, X.-Y.: A Description of the Advanced Research WRF Model Version 4, 2021.

Stolz, S., Adams, N. A., and Kleiser, L.: The approximate deconvolution model for large-eddy simulations of compressible flows and its application to shock-turbulent-boundary-layer interaction, Physics of Fluids, 13, 2985–3001, https://doi.org/10.1063/1.1397277, 2001.

710 Sullivan, P., Horst, T., Lenschow, D., Moeng, C.-H., and Weil, J.: Structure of Subfilter-Scale Fluxes in the Atmospheric Surface Layer with Application to Large-Eddy Simulation Modelling, Journal of Fluid Mechanics, 482, https://doi.org/10.1017/S0022112003004099, 2003.

Sun, J., Burns, S. P., Lenschow, D. H., Banta, R., Newsom, R., Coulter, R., Frasier, S., Ince, T., Nappo, C., Cuxart, J., Blumen, W., Lee, X., and Hu, X.-Z.: Intermittent Turbulence Associated with a Density Current Passage in the Stable Boundary Layer, Boundary-Layer Meteorology, 105, 199–219, https://doi.org/10.1023/A:1019969131774, 2002.

Sun, J., Nappo, C. J., Mahrt, L., Belušić, D., Grisogono, B., Stauffer, D. R., Pulido, M., Staquet, C., Jiang, Q., Pou-
715 quet, A., Yagüe, C., Galperin, B., Smith, R. B., Finnigan, J. J., Mayor, S. D., Svensson, G., Grachev, A. A., and Neff, W. D.: Review of wave-turbulence interactions in the stable atmospheric boundary layer, Reviews of Geophysics, 53, 956–993, https://doi.org/https://doi.org/10.1002/2015RG000487, 2015.

van der Laan, M. P. and Sørensen, N. N.: Why the Coriolis force turns a wind farm wake clockwise in the Northern Hemisphere, Wind Energy Science, 2, 285–294, https://doi.org/10.5194/wes-2-285-2017, 2017.

720 van der Linden, S. J. A., van de Wiel, B. J. H., Petenko, I., van Heerwaarden, C. C., Baas, P., and Jonker, H. J. J.: A Businger Mechanism for Intermittent Bursting in the Stable Boundary Layer, Journal of the Atmospheric Sciences, 77, 3343 – 3360, https://doi.org/10.1175/JAS-D-19-0309.1, 2020.

Vanderwende, B. J., Lundquist, J. K., Rhodes, M. E., Takle, E. S., and Irvin, S. L.: Observing and Simulating the Summertime Low-Level Jet in Central Iowa, Monthly Weather Review, 143, 2319–2336, https://doi.org/10.1175/MWR-D-14-00325.1, 2015.

725 Wise, A. S., Neher, J. M. T., Arthur, R. S., Mirocha, J. D., Lundquist, J. K., and Chow, F. K.: Meso- to microscale modeling of atmospheric stability effects on wind turbine wake behavior in complex terrain, Wind Energy Science, 7, 367–386, https://doi.org/10.5194/wes-7-367-2022, 2022.

Wise, A. S., Arthur, R. S., Abraham, A., Wharton, S., Krishnamurthy, R., Newsom, R., Hirth, B., Schroeder, J., Moriarty, P., and Chow, F. K.: Large-eddy simulation of an atmospheric bore and associated gravity wave effects on wind farm performance in the southern Great Plains,
730 Wind Energy Science, 10, 1007–1032, https://doi.org/10.5194/wes-10-1007-2025, 2025.

Wong, V. C. and Lilly, D. K.: A comparison of two dynamic subgrid closure methods for turbulent thermal convection, Physics of Fluids, 6, 1016–1023, https://doi.org/10.1063/1.868335, 1994.

Zang, Y., Street, R., and Koseff, J.: A Dynamic Mixed Subgrid-Scale Model and Its Application to Turbulent Recirculating Flows, Physics of Fluids A: Fluid Dynamics, 5, 3186, https://doi.org/10.1063/1.858675, 1993.

735 Zhou, B. and Chow, F. K.: Large-Eddy Simulation of the Stable Boundary Layer with Explicit Filtering and Reconstruction Turbulence Modeling, Journal of the Atmospheric Sciences, 68, 2142–2155, https://doi.org/10.1175/2011JAS3693.1, 2011.

Zhou, B. and Chow, F. K.: Turbulence Modeling for the Stable Atmospheric Boundary Layer and Implications for Wind Energy, Flow, Turbulence and Combustion, 88, 255–277, https://doi.org/10.1007/s10494-011-9359-7, 2012.

Zhou, B. and Chow, F. K.: Nested Large-Eddy Simulations of the Intermittently Turbulent Stable Atmospheric Boundary Layer over Real
740 Terrain, Journal of the Atmospheric Sciences, 71, 1021 – 1039, https://doi.org/10.1175/JAS-D-13-0168.1, 2014.